MORC2 Mediates Transcriptional Regulation Through Liquid-Liquid Phase Separation

Yanshen Zhang[1,2,3,#], Weiya Xu[1,2,#], Wenxiu Duan[1,2,#], Yu Wei[1,2,3],Wenli Jiang[1,2,3], Feng Zhu[1], Chengdong Huang[1,2,*], Chao Wang[1,2,3*], and Yihui Bi[4*]

[1]Hefei National Research Center for Physical Sciences at the Microscale, Center for Advanced Interdisciplinary Science and Biomedicine of IHM, Division of Life Sciences and Medicine, University of Science and Technology of China, Hefei, China.

[2]Ministry of Education Key Laboratory for Membraneless Organelles and Cellular Dynamics, Biomedical Sciences and Health Laboratory of Anhui Province, Division of Life Sciences and Medicine, University of Science and Technology of China, Hefei, China.

[3]Department of Neurology, the First Affiliated Hospital of USTC, Division of Life Sciences and Medicine, University of Science and Technology of China, Hefei, China.

[4]Department of Orthopedics, The Second Affiliated Hospital of Anhui Medical University, Hefei, China.

Running title: Multivalent interactions and DNA binding underlie phase separation of MORC2

[#]These authors contributed equally to this work.

[*]Corresponding authors: Chengdong Huang (huangcd@ustc.edu.cn);

Chao Wang (cwangust@ustc.edu.cn);

Yihui Bi (yihuibi@ahmu.edu.cn).

Abstract

MORC2 is a chromatin-associated ATPase essential for transcriptional silencing and genome stability, yet the biophysical principles governing its regulatory activity remain elusive. Here, we demonstrate that full-length MORC2 undergoes biomolecular condensation to form dynamic nuclear assemblies, a process fundamentally required for its repressor function. Endogenous MORC2 forms discrete, dynamic condensates in neurons from *EGFP-MORC2* knock-in mice, supporting the physiological relevance of these assemblies *in vivo*. Mechanistically, a 3.1 Å crystal structure of coiled-coil 3 (CC3) identifies a dimeric scaffold that serves as a structural hub, while multivalent 'sticker' interactions between an intrinsically disordered region (IDR) and a newly defined IDR-binding domain (IBD) drive condensation. We show that DNA acts as a molecular scaffold that triggers MORC2 condensation, which in turn allosterically stimulates its ATPase activity. Critically, by employing a “killswitch” strategy to decouple assembly from internal fluidity, we reveal that only dynamic MORC2 condensates—not static aggregates or condensation-deficient mutants—can restore transcriptional repression in MORC2-knockout cells. Furthermore, pathogenic variants linked to CMT2Z and SMA differentially perturb these material properties and enzymatic turnover, providing a mechanistic link between condensate dysregulation and human neuropathies. Together, our findings establish a DNA-templated condensation mechanism for MORC2 and provide a molecular framework for understanding how the material state of chromatin-associated machinery dictates gene regulation and disease pathogenesis

Introduction

Chromatin dynamically regulates DNA accessibility to orchestrate essential processes such as transcription, replication, and DNA repair[1–5]. These processes are dynamically regulated by chromatin-associated complexes, such as the human silencing hub (HUSH) complex[6], which control the accessibility of genetic material to regulatory machinery. The Microrchidia (MORC) protein family, characterized by a conserved N-terminal GHL-ATPase domain and a structurally diverse C-terminal region, regulates gene expression and chromatin organization[7–10]. These C-terminal domains are thought to contribute to dimerization and functional specificity[11–14]. Notably, MORC2 has been identified as a component of the HUSH complex and is required for HUSH-mediated transcriptional repression[12].

GHL ATPases, including DNA gyrase, Hsp90, and MutL, rely on ATP-dependent dimerization to drive conformational changes essential for substrate engagement and enzymatic regulation[15–19]. Similar mechanisms have been proposed for MORC family members. In humans, the MORC family comprises five members—MORC1, MORC2, MORC3, MORC4, and SMCHD1, and different MORC paralogs target distinct genomic loci, including transposable elements, viral DNA, and long-exon genes[7,20,21]. The conserved N-terminal GHL-ATPase domain of MORC family proteins has been extensively characterized, whereas the evolutionarily diversified, multi-domain C-terminal regions are thought to act as key determinants of chromatin targeting and functional specificity. Despite these shared structural features, the molecular basis for MORC-mediated transcriptional regulation remains poorly understood, partly due to limited structural insight into the full-length proteins and C-terminal regions.

MORC2 has recently been identified as a key regulator of chromatin architecture and gene silencing, primarily through its recruitment to HUSH-target loci via C-terminal CC2 domain-mediated interactions with TASOR and MPP8[12]. While its silencing activity was initially attributed to the N-terminal ATPase domain, genetic complementation studies have revealed that the CW domain and all three coiled-coil (CC) regions are also indispensable for its function[12,13]. Beyond its structured domains,

sequence analyses and structural predictions have uncovered an extended intrinsically disordered region (IDR) spanning the central to C-terminal regions of the protein, suggesting potential regulatory mechanisms by facilitating multivalent and dynamic interactions beyond enzymatic activity[22].

Transcriptional silencing is frequently spatially organized within membrane-less nuclear compartments, often driven by the process of biomolecular condensation[23,24]. Sequence analyses of MORC2 reveal an extended intrinsically disordered region (IDR) spanning the central to C-terminal domains, suggesting a capacity for the multivalent, weak interactions that underpin phase separation[25,26]. While IDRs are common in chromatin-associated proteins, their presence alone does not guarantee condensation; rather, phase separation often emerges from the coordinated interplay between disordered segments and structured oligomerization hubs. How such mesoscale organization modulates MORC2's enzymatic turnover and its ability to remodel the genome remains a fundamental question in the field.

In this study, we demonstrate that MORC2 undergoes phase separation to form dynamic nuclear condensates. We define the structural basis for this behavior, identifying a dimeric CC3 scaffold that, together with multivalent interactions between the IDR and a newly identified IDR-binding domain (IBD), drives condensation. We further show that DNA binding acts as a molecular scaffold to promote MORC2 assembly, which in turn allosterically enhances its ATPase activity. Using a combination of cellular "killswitch" assays and *in vivo* models, we establish that the dynamic material properties of MORC2 condensates—rather than mere protein recruitment—are strictly required for transcriptional regulation. Finally, we provide mechanistic insights into how neuropathic disease-associated mutations in the MORC2 N-terminus perturb this biophysical balance, linking condensate dysregulation to human pathology.

Results

Coiled-coil 3 (CC3) mediates dimerization of full-length MORC2

To determine whether MORC2 has N- and C-terminal dimerization interfaces similar to those in other GHL-type ATPases[27], which previously identified the role of CC3 (previously designated as CC4) in MORC2 dimerization[14], we established an *in vitro* system to purify full-length (FL) human MORC2 (MORC2FL, residues 1-1032) from HEK293F cells, yielding nucleic acid-free, highly pure proteins for structural and functional analyses (Fig. 1a, b). Analytical size-exclusion chromatography coupled with static light scattering (SLS) demonstrated that MORC2FL forms dimers, with a molecular weight of approximately 239 ± 1 kDa under buffer conditions containing 1000 mM NaCl even in the absence of ATP (Fig. 1c). Notably, the addition of 601 DNA resulted in a detectable increase in molecular weight (303 ± 2 kDa), indicative of DNA-protein complex formation, but did not disrupt the dimeric assembly of MORC2 in the same buffer condition (Fig. 1c).

To elucidate the atomic structure of MORC2FL, we initially employed negative-stain electron microscopy to reveal that MORC2FL particles were poorly resolved and exhibited considerable heterogeneity in buffer containing 300 mM NaCl. Notably, a subset of particles displayed a morphology consistent with dimer formation (Fig. S1a). To further investigate this, we performed structural prediction of MORC2FL using AlphaFold3 and identified a predicted structure that closely resembled the observed reconstruction (Fig. S1b). We then examined the oligomerization properties of various MORC2 constructs. MORC2$^{1\text{-}900}$ (FLΔCC3-IBD domain) was found to exist as a monomer, whereas MORC2$^{901\text{-}1032}$ and MORC2$^{901\text{-}1003}$ exhibited dimeric properties, confirming the critical role of the CC3 domain (residues 901-1003) in mediating MORC2 dimerization (Fig. 1c, and Fig. S1c).

To gain further structural insights, we determined the 3.1 Å crystal structure of the CC3 dimer using X-ray diffraction (Table S1). The structure revealed that the dimer interface is stabilized predominantly by hydrophobic interactions. Three key

hydrophobic residues—L911, L915, and F922—form distinct layers within the dimer interface (layers 1-3, Fig. 1e, and Fig. S1e, f). The side chains of these residues are buried within the dimerization interface, creating a hydrophobic core critical for maintaining the stability of the dimer.

We systematically introduced single-point mutations in these hydrophobic residues to assess their contributions to dimerization. SLS analysis demonstrated that the wild-type (WT) MORC2$^{901-1032}$ (with Trx-tag) fragment predominantly exists as a dimer (~61 kDa). In contrast, all three key mutants (L911Q, L915Q, and F922Q) displayed altered molecular weight distributions indicative of disrupted dimer formation and enhanced higher-order oligomerization (more than 61 kDa) (Fig. S1g). However, none of these mutations completely disrupted dimerization or converted the dimer to a monomeric state (Fig. S1g). Further analyses of additional single-site mutants (e.g., I908Q, Y921A, F951Q, Y954A, L958Q) showed minimal effects on dimer stability, underscoring the central importance of L915 and its neighboring hydrophobic layers in stabilizing the CC3 dimer (Fig. S1g). Moreover, we examined the dimeric status of truncated CC3 constructs (residues 901-975), which confirmed that the CC3 N-terminal region is sufficient to drive dimer formation (Fig. 1f). To delineate the structural basis of these interactions, we mapped the positions of hydrophobic residues within the CC3 backbone (Fig. S1e). The distances between interacting residues, such as I908-I908' (3.4 Å), L911-L915' (3.7 Å), F922-F922' (3.9 Å), and L958-L958' (4.0 Å), revealed a tightly packed hydrophobic network. The robustness of this network ensures the integrity of the CC3 dimer, even under varying salt concentration and protein concentration tested *in vitro* conditions. These findings collectively suggest that the CC3 domain plays a critical role in MORC2 dimerization. The dimeric assembly of CC3 is essential for maintaining the structural integrity of the protein, which likely underpins its functional activities, including associations with chromatin[14].

MORC2 forms condensates both *in vivo* and *in vitro*

In the predicted structure of MORC2FL, we observed an extended unstructured

region at the C-terminus of the protein (Fig. S1b). This region is classified as an intrinsically disordered region (IDR), a protein architecture frequently reported to facilitate multivalent interactions and can act as a scaffold for phase separation[25, 28]. Specifically, IUPred2A analysis predicts that the residues 593-735 predominantly exhibit high disorder scores, prompting us to define this segment as the IDR domain (Fig. 1a).

In vitro, sedimentation assays showed that when the salt concentration was reduced to 150 mM, more than half of the EGFP fused MORC2FL (EGFP-MORC2FL) precipitated into the pellet fraction (Fig. 2a, b). Fluorescence imaging revealed that at this near-physiological ionic strength, EGFP-MORC2FL spontaneously demixed to form well-defined spherical droplets (Fig. 2c, d). These droplets exhibited a characteristic polydispersity in size and showed significant coarsening as protein concentration increased (Fig. S2a). Sedimentation assays further showed that the pellet fraction of EGFP-MORC2FL after centrifugation was concentration-dependent (Fig. S2b). The EGFP-MORC2FL-enriched condensates exhibited dynamic behavior, including droplet fusion (Fig. S2c) and fluorescence recovery after photobleaching (FRAP) (Fig. 2e, f), indicating a dynamic state.

Using antibody labeling, we observed that endogenous MORC2 forms discrete, dense punctate structures within the nuclei of HeLa cells (Fig. 2g). The specificity of these puncta was confirmed by their absence in MORC2-knockout (KO) HeLa cells (Fig. S2d, e), suggesting that MORC2 may natively organize into higher-order nuclear condensates under physiological conditions. To further characterize these assemblies, we transfected HeLa cells with EGFP-MORC2FL and observed the formation of prominent, droplet-like nuclear condensates (Fig. 2h). Notably, consistent with the endogenous staining patterns, EGFP-MORC2FL condensates preferentially localized to regions of reduced chromatin density, as visualized by the H2A-mCherry signal. This distinct spatial distribution implies a potential role for MORC2 condensates in organizing or regulating the heterochromatin landscape. FRAP analysis of these EGFP-MORC2FL puncta revealed fluorescence recovery on a timescale of seconds (Fig. 2i, j). Furthermore, these puncta underwent active fusion events (Fig. S2f), a

hallmark of dynamic liquid-like condensates with a highly mobile internal environment.

To determine whether MORC2 forms biomolecular condensates under physiological conditions, we generated mice expressing EGFP-MORC2 protein from the endogenous locus (Fig. S3a). We focus on neurons in the brain and spinal cord as missense mutations in *MORC2* cause neuropathies including Charcot-Marie-Tooth and spinal muscular atrophy disease[11,13]. Imaging of NeuN-positive neurons revealed that EGFP-MORC2FL condensates occur in neurons under endogenous expression level (Fig. 2k). FRAP analysis in freshly prepared brain slices further demonstrated rapid and partial fluorescence recovery, supporting the dynamic nature of endogenous MORC2 assemblies (Fig. 2l). In addition, unlike MORC3, which shows cell cycle-dependent nuclear puncta formation[29], MORC2 condensates were absent in mitotic cells (Fig. S3b). Together, these results indicate that MORC2 forms phase-separated biomolecular condensates under physiological conditions *in vivo* and *in vitro*.

The MORC2 C-terminal domain (CTD) drives condensate formation

To identify the key determinants governing the assembly of MORC2 nuclear condensates, we partitioned the protein into two functional modules based on its domain architecture: the N-terminal domain (NTD, residues 1–472), comprising the ATPase and CC1 motifs, and the C-terminal domain (CTD, residues 473–1032), which encompasses the IDR and multiple coiled-coil regions. A series of EGFP-tagged truncation constructs were then expressed in HeLa cells to systematically map the regions essential for condensate formation (Fig. 3a). Deletion of the CTD completely abolished puncta formation, resulting in a diffuse localization across the nucleus and cytoplasm (Fig. S4a). By contrast, NTD deletion had negligible effects on nuclear localization or the capacity for condensation. To exclude the possibility that the NTD's diffuse pattern was merely due to its loss of nuclear entry, we appended an exogenous nuclear localization signal (NLS, PKKKRKV[30]) to the NTD; however, while this redirected the protein to the nucleus, it failed to restore

puncta (Fig. 3a), confirming that the CTD is the primary driver of MORC2 condensation. To assess whether the CTD is intrinsically prone to undergo condensation *in vitro*, we purified a CTDΔCW (residues 537–1032) variant from *E. coli*, as the full CTD exhibited suboptimal biochemical stability (Fig. S5a, b). At 150 mM NaCl, Cy3-labeled CTDΔCW readily formed discrete condensates in a concentration-dependent manner (Fig. 3b, c), and displayed a sedimentation profile characteristic of phase-separated assemblies (Fig. 3d, e). Fluorescence microscopy and static light scattering (SLS) confirmed that Cy3 labeling did not perturb its condensation behavior, morphology, or molecular weight distribution (Fig. S5c–f).

Further dissection of the CTD revealed that deletion of either the CC2 or TCD domains did not impair the formation of nuclear puncta (Fig. S4b). In contrast, removal of the IDR-NLS region (residues 593-761) abolished both puncta formation and nuclear localization (Fig. S4b). Notably, appending an exogenous NLS (PKKKRKV) to CTDΔIDR-NLS restored its nuclear entry but failed to rescue condensate assembly (Fig. S4c), identifying the IDR as a prerequisite for condensation. Similarly, deletion of the CC3-IBD segment maintained nuclear localization but eliminated puncta formation, indicating that this region is also indispensable (Fig. S4b). Intriguingly, neither the IDR-NLS fragment nor the CC3-IBD fragment alone (even when NLS-fused) was sufficient to trigger condensation (Fig. S4d), implying a cooperative mechanism between these modules. Consistent with these cellular findings, *in vitro* assays showed that neither the MORC2ΔCC3-IBD (residues 1–900) nor the isolated CC3-IBD fragment could undergo condensation (Fig. S6a-b). However, mixing the IDR with the IBD fragment reconstituted robust condensate formation at higher concentration (Fig. S6c), confirming their synergistic role. Finally, the CW domain appears to modulate condensate morphology, as its deletion led to enlarged and frequently fused puncta. We conclude that the IDR, CC3, and IBD constitute the minimal structural core required for MORC2 condensation, while the CW domain serves to restrict condensate overgrowth and maintain proper morphology (Fig. 3a, and Fig. S4e).

Multivalent interactions between the IDR and IBD promote MORC2 condensation

Next, we elucidated the mechanistic basis for MORC2 assembly mediated by the IDR and CC3-IBD. We hypothesized that multivalent interactions between these modules drive the formation of a condensed phase that coexists with a dilute aqueous phase. Using nuclear magnetic resonance (NMR) spectroscopy, we characterized the interaction between the IDR and the C-terminal segment (residues 901–1032). ^{15}N-HSQC titration assays using the ^{15}N-labeled CC3 (residues 901-1003) or the 1004-1032 fragment revealed that residues 1004-1032 constitute the primary binding site for the IDR, which we termed the IDR-Binding Domain (IBD), whereas the CC3 region exhibited negligible interaction (Fig. 4a-c).

Further subdivision of the IDR into three segments—IDRa (residues 593-643), IDRb (residues 644-694), and IDRc (residues 695-735)—pinpointed IDRa as the key region responsible for interaction with IBD (Fig. 4a, d-f). As is typical for IDR-mediated interactions involved in condensation, the observed chemical shift perturbations (CSPs) were relatively small but highly region-specific. Notably, the CSP profile of IDRa closely mirrors that of the full-length IDR, whereas IDRb and IDRc showed minimal perturbations (Fig. S7). Detailed sequence analysis revealed that the CSPs are clustered around charged residues (D, E, K, R) and their neighboring residues (Y, T, N, I, L, P). This suggests that the association is driven by a concerted action of multiple non-covalent forces: beyond the foundational electrostatic attraction, the involvement of aromatic (Y) and aliphatic (I, L, P) residues points to the contribution of π-π stacking, cation-π interactions, and hydrophobic effects, while polar residues (T, N) likely facilitate intermolecular hydrogen bonding. This hierarchical assembly, characterized by both charge complementarity and hydrophobic-like contributions, aligns with the 'sticker-and-spacer' model. In this framework, these multivalent residues act as 'stickers' that provide the requisite valency to scaffold a robust yet dynamic network, while the intervening sequences serve as 'spacers' to maintain the fluidity necessary for the condensed state (Fig. 4g). Collectively, these quantitative CSP data support a

model of weak, dynamic, and region-specific interactions, a hallmark of IDR-driven condensation mechanisms[31–33].

To assess the role of IDRa-IBD multivalent interactions in cells, we transfected HeLa and HEK293T cells with MORC2FL variants harboring individual deletions of the IBD, IDRa, IDRb, or IDRc regions. Deletion of the IBD abolished condensate formation in both HeLa cells (Fig. 3a, and Fig. S4e) and HEK293T cells (Fig. S8). Similarly, deletion of IDRa significantly impaired condensation, resulting in a marked decrease in both the number and area of nuclear puncta, whereas IDRb or IDRc deletions had minimal impact (Fig. 4h, i). Based on these findings, we propose a model in which multivalent 'sticker' interactions between IDRa and the IBD drive MORC2 intermolecular assembly, a process further potentiated by CC3-mediated dimerization, which collectively provides the valency threshold required for condensation (Fig. 4j).

DNA binding promotes MORC2 condensation and stimulates ATPase activity

Notably, MORC2 condensates form exclusively within the nuclei of transfected HeLa cells, implying that chromatin-associated factors—most likely DNA—serve as essential cues for their nucleation or stabilization. While the N-terminal CC1 domain was previously identified as a DNA-binding module[13], we hypothesized that the full-length MORC2 architecture utilizes additional interfaces to facilitate complex chromatin interactions.

To test this, we performed a comprehensive domain screen using electrophoretic mobility shift assays (EMSA). Beyond confirming the robust DNA-binding activity of the CC1 domain (Fig. 5a, b), our screen revealed that the CC2, IDR, and TCD (Tudor Chromo-like domain) also possess significant DNA-binding capabilities (Fig. 5c-e). In contrast, the CC3–IBD fragment showed no affinity for DNA (Fig. 5f). These results indicate that MORC2 employs a multivalent DNA-binding architecture distributed across both its N-terminal and C-terminal regions.

Building on this, we investigated whether these multivalent DNA-protein interactions could scaffold MORC2 condensation *in vitro*. At 0.9 μM, MORC2FL

alone failed to form discrete assemblies; however, the addition of 25 nM 601 DNA induced robust condensate formation, demonstrating that DNA acts as a molecular seed to promote MORC2 phase separation (Fig. 5g, h). Interestingly, while the NTD (residues 1–536) binds DNA, it remains diffuse (Fig. S6d,e), whereas the CTDΔCW (residues 537–1032) undergoes DNA-driven condensation (Fig. 5i). Systematic evaluation across a matrix of protein and DNA concentrations yielded a phase diagram mapping the transitions between clear solutions, liquid-like condensates, and amorphous precipitates, consistently showing that DNA significantly lowers the concentration threshold for MORC2 condensation (Fig. S9). This functional divergence suggests a division of labor within MORC2: while multiple domains provide DNA affinity, the CTD provides the essential protein-protein interaction network required for higher-order assembly.

Finally, we explored how this assembly impacts the MORC2 enzymatic core. The addition of 601 DNA markedly stimulated the ATPase activity of wild-type MORC2, but not the ATP-binding-deficient N39A mutant (Fig. 5j). This reveals a synergistic interplay: DNA binding does not merely recruit MORC2 to chromatin; it acts as a molecular scaffold that facilitates condensation, which in turn may optimize the productive conformation or local density required for allosteric activation of the ATPase domain. In conclusion, these findings highlight a coordinated mechanism that integrates DNA binding, condensation, and enzymatic activity, providing a biophysical basis for the multivalent assembly and allosteric regulation of MORC2 on chromatin.

Condensate formation and dynamics are required for MORC2-mediated transcriptional regulation

Establishing a causal link between biomolecular condensation and biological function—particularly in transcriptional regulation—remains a central challenge. A key question is whether MORC2 condensates represent discrete functional entities or merely inactive byproducts. To address this, we sought to decouple condensate formation from internal dynamics, allowing for a rigorous interrogation of their

functional relevance. While deletion of the CC3 domain abolishes MORC2 condensation, CC3 is also indispensable for dimerization, confounding functional interpretations. Furthermore, although deleting IDRa markedly weakens MORC2 condensation, a tool to specifically manipulate the solubility and internal mobility of these assemblies was previously lacking.

To overcome these limitations, we employed a micropeptide-based 'killswitch' (KS) strategy fused to the C-terminus of MORC2 (Fig. 6a). This approach selectively reduces condensate dynamics without disrupting protein expression, folding, or domain architecture[34]. Unlike the ΔCC3 or ΔIDRa mutants, the MORC2+KS variant robustly form nuclear condensates but exhibits markedly reduced internal dynamics, as demonstrated by FRAP analyses showing minimal fluorescence recovery (Fig. 6b, c). This strategy allowed us to perturb the material properties of the condensates independently of structural integrity.

To evaluate how the modulation of MORC2 condensates influences its gene regulatory capacity, we compared the transcriptional consequences of rescuing MORC2-knockout HeLa cells with MORC2FL, condensation-deficient mutants (ΔCC3 and ΔIDRa), and the dynamics-defective MORC2+KS (Fig. 6d). Bulk RNA-seq was performed 48 hours post-transfection. We hypothesized that impairing either the assembly or the fluidity of the condensates would compromise MORC2-dependent gene regulation. Notably, despite being expressed at substantially higher levels than MORC2FL (Fig. 6e), all three mutants showed a striking and consistent failure to restore the MORC2-dependent transcriptional profile (Fig. 6f–h). This defect was particularly pronounced for transcriptionally repressed genes, including two sets of high-confidence MORC2 targets identified in prior studies[12, 22] (Fig. 6i, and Fig. S10). Gene Ontology analysis revealed that the MORC2-regulated genes are involved in DNA damage responses, viral infection, and cell cycle regulation (Fig. 6g). These findings demonstrate that neither increased protein abundance nor the mere presence of static, condensate-like structures is sufficient to restore MORC2 function.

Collectively, these data support a model in which the dynamic nature of MORC2

condensates is essential for full transcriptional activity. While soluble MORC2 complexes are likely involved in initial target recognition, our results indicate that proper condensate formation—and critically, internal fluidity—are required for effective transcriptional control. The inability of the MORC2+KS mutant to rescue transcriptional defects, despite forming visible nuclear assemblies, strongly argues against a model where MORC2 condensates are merely inert byproducts of its activity.

Pathogenic MORC2 variants differentially modulate condensation, DNA binding, and ATPase activity

MORC2 is essential for gene silencing at H3K9me3-marked loci and retrotransposon repression[6,35–37]. Pathogenic mutations in its GHL-type ATPase domain have been linked to severe neuropathies and cancer[38–42]. To explore whether these mutations influence the condensation behavior and biochemical activities of the full-length protein, we examined a panel of disease-associated variants, including those linked to Charcot–Marie–Tooth disease type 2Z (CMT2Z: E236G, R252W, Q400R, D466N) and spinal muscular atrophy (SMA: S87L, S218L, F256L, R266A, T424R) (Fig. 7a).

In HeLa cells, all variants retained the ability to form nuclear puncta. However, the CMT2Z-linked E236G and, notably, the SMA-linked T424R mutants significantly increased the proportion of cells exhibiting nuclear condensates (Fig. 7b). These observations suggest that the N-terminal region plays a nuanced role in modulating the phase boundary of MORC2. Specifically, previous structural studies indicated that the T424R mutation has minimal effects on the overall N-terminal architecture but primarily alters the assembly and dissociation kinetics of the N-terminal dimer[13]. This suggests that the conformational cycling or dimerization state of the N-terminus directly contributes to the macroscopic regulation of MORC2 condensates. Interestingly, while deletion of the N-terminal region did not abolish puncta formation, FRAP analyses revealed a marked loss of condensate fluidity compared with the full-length protein (Fig. S11). This highlights the N-terminus as a critical regulator of

the material properties of MORC2 assemblies. Consequently, we evaluated the dynamics of E236G and T424R condensates; FRAP measurements showed substantially reduced recovery for E236G, indicating decreased internal fluidity, whereas T424R exhibited minimal effects (Fig. 7e, f).

In vitro ATPase assays revealed that T424R significantly increases enzymatic activity (Fig. 7c), consistent with its reported role in promoting ATPase dimer cycling[13]. Additionally, S218L and F256L variants enhanced ATP hydrolysis, whereas others, such as Q400R and D466N, showed activity comparable to WT (Fig. 7c). Due to severe solubility issues, E236G could not be biochemically characterized *in vitro* (Fig. S12e).

We next assessed DNA binding affinity of MORC2 variants using fluorescence polarization (FP) assays. Despite subtle differences, none of the variants showed statistically significant changes in DNA-binding capacity (Fig. 7d), indicating that these mutations primarily perturb enzymatic turnover and condensation dynamics rather than DNA recruitment.

In summary, our results support a model in which MORC2 mediates transcriptional regulation through its intrinsic ability to undergo biomolecular condensation. The N-terminal ATPase domain undergoes conformational cycling between open and closed states, while the C-terminal CC3-mediated dimer acts as a stable scaffold for condensate formation (Fig. 7g). MORC2 condensation is further fine-tuned by multivalent interactions between the IBD and IDRa regions, as well as by DNA binding. Together, these features enable MORC2 to bridge distal chromatin regions and establish repressive condensates, underscoring its central role in chromatin organization and genome stability

Discussion

Biophysical Principles of MORC2 Organization

While the MORC family of ATPases is recognized as a central player in epigenetic regulation[43], genome stability[44,45], and meiotic progression[46,47], the biophysical

principles governing their spatiotemporal organization have remained elusive. In this study, we establish a causal link between MORC2 condensation and its transcriptional regulatory function. By integrating high-resolution structural insights with functional assays, we reveal that MORC2 does not act merely as a solitary chromatin remodeler[3,5,48]; instead, it functions as phase separation-driven DNA compaction machinery. This discovery demonstrates how mesoscale material properties—specifically the fluidity and density of protein-DNA assemblies—are directly translated into precise gene regulation.

A Modular Engine for Condensate Assembly

The architectural basis of MORC2 assembly relies on a finely tuned multi-domain interplay. The C-terminal region, comprising the structured CC3-IBD and the intrinsically disordered IDR, provides the mechanistic engine for this process. CC3 serves as a critical structural scaffold (Fig. 1e, and 3a), mediating homodimerization that effectively doubles the molecular valency, thereby facilitating multivalent "sticker" interactions between the IDR and the defined IBD (Fig. 4). We found that mutations selectively abrogating condensate formation, or those that arrest condensate dynamics without blocking assembly, impair MORC2's ability to repress core target genes (Fig. 6). This underscores that high internal fluidity is functionally paramount, ensuring the rapid exchange kinetics required for continuous ATP hydrolysis and dynamic chromatin engagement.

The "Viscoelastic Window" and Molecular Stoichiometry

A defining insight from our study is that the mere presence of nuclear puncta is insufficient for MORC2's repressor activity. Instead, its function is governed by the precise material state of the condensates. We demonstrate that DNA acts as an essential functional scaffold (Fig. 5), driving condensation potentially mediated by nonspecific electrostatic interactions with the arginine/lysine-rich IDR. Crucially, these assemblies are exquisitely sensitive to molecular stoichiometry. This establishes a narrow, functionally permissive "viscoelastic window": Too Diffuse: MORC2 fails

to achieve the local density necessary for mechanical DNA compaction. Too Rigid: If the system crosses the threshold into a solid-like, arrested state (as seen in the MORC2 +KS mutant or E236G variant), it loses the fluidity required for enzymatic turnover and co-repressor engagement. Within the nucleus, the CW domain likely serves as a regulatory node, orchestrating the compositional regulation of these condensates by reading specific epigenetic marks to fine-tune local valency and morphology (Fig. 3 and Fig. S3).

Mechanistic Insights into Pathogenic Variants

Our analysis of disease-associated variants—particularly E236G (CMT2Z) and T424R (SMA)—highlights how mutations in the ATPase domain can pleiotropically affect both enzymatic turnover and phase behavior (Fig. 7). While T424R primarily accelerates the ATPase dimer cycle[13], E236G triggers a transition toward a less dynamic, "hardened" condensate state. These results emphasize that disease mutations do not simply "turn off" the protein; they perturb the biophysical context of the assembly. The observation that some variants exhibit elevated ATPase activity *in vitro* suggests that in the native cellular environment, condensation-mediated local enrichment may be required to properly couple ATP hydrolysis to productive chromatin remodeling.

Our findings clarify previous discrepancies regarding MORC2's DNA binding. By utilizing the 601 nucleosome-positioning sequence, we demonstrate a much more robust interaction than previously captured with short, random dsDNA. Furthermore, the use of full-length MORC2 reveals that C-terminal regulatory domains are essential for maintaining enzymatic homeostasis—a feature masked in truncated constructs. Whether MORC2-mediated silencing is achieved through direct modulation of ATPase cycles or an independent mechanical compaction mechanism remains an open question.

While our study establishes the essential role of MORC2 condensation in

transcriptional control, this exploration represents an initial step toward deciphering the complex coordination between enzymatic turnover and phase behavior. Future research is required to resolve how the ATP-dependent “DNA clamp” cycle is spatially coupled to the physical compaction of chromatin, and whether additional co-repressors are selectively partitioned into these dynamic assemblies to maintain epigenetic stability.

Materials and Methods

Plasmid construction, cell culture and transfection

WT MORC2 (UniProt: Q9Y6X9) cDNA was amplified from a cDNA library derived from HeLa cells via reverse transcription. The MORC2 cDNA was then subcloned into the p3xFLAG-Myc-CMV-24 vector between BglII and KpnI restriction sites using seamless cloning. The seamless cloning process was facilitated by the ClonExpress II One-Step Cloning Kit (Vazyme, #C112-02) according to the manufacturer's instructions. An EGFP sequence was subsequently inserted into the BglII site at the N-terminal of MORC2 to generate the EGFP-MORC2 construct. To generate deletion mutant constructs of MORC2 for intracellular studies, specific regions of MORC2 were targeted and deleted using a polymerase chain reaction (PCR)-based approach. An 18- or 21 bp homologous sequence originating from one of the forward or reverse primers was introduced into the other primer, and the resulting PCR products were subjected to homologous recombination cloning, facilitated by the 18-bp homologous sequence. For protein expression and purification, MORC2FL and truncated MORC2 were cloned into prokaryotic expression vectors with MBP or Trx fusion proteins for bacterial expression.

In addition, MORC2FL and a series of truncation mutants were purified using a HEK293F eukaryotic expression system for *in vitro* phase separation and static light scattering (SLS) assays. A260/280 measurements, agarose gel analysis, or EMSA information on protein purifications and their experimental applications in this study is provided in Table S2. HeLa, HEK293T cells were cultured in DMEM medium (Biological Industries, DMEM, high re maintained in a humidified incubator at 37°C with 5% CO_2. Cell transfection was performed using Lipofectamine 3000 (Invitrogen) according to the manufacturer's instructions. Briefly, cells were seeded in appropriate culture plates the day before transfection and allowed to reach 40-60% confluency. The separately diluted Lipofectamine 3000 reagent and plasmids in Opti-MEM reduced serum medium (Gibco) were mixed, and the transfection complexes were

added to cells after 20 minutes. After a 6-hour incubation, the transfection medium was replaced with fresh complete DMEM medium.

Recombinant protein expression, purification

Plasmids containing His-tagged genes were transformed into *E. coli* BL21 (DE3) cells and cultured in Luria-Bertani medium with 50 mg/L ampicillin. When the culture reached an optical density (OD) of 0.6-0.8 at 600 nm, the temperature was lowered to 16°C. Isopropyl β-D-1-thiogalactopyranoside (IPTG) (0.25 mM) was added to induce protein expression for 18-20 hours. Cells were harvested by centrifugation at 13,000 × g for 15 minutes, then resuspended in Buffer A (50 mM Tris-HCl, pH 8.0, 1000 mM NaCl, 10 mM imidazole, 1 mM dithiothreitol (DTT), and 1 mM phenylmethylsulfonyl fluoride (PMSF)). The cell suspension was snap-frozen and stored at -80°C for subsequent protein purification. HEK293F suspension-adapted cells were cultured in conical flasks at 37°C, 120 rpm, and 5% CO_2, until a density of 1.0 × 10□ cells/mL was reached. The cells were transiently transfected with 1 mg of MORC2-6 × His plasmid using 2 mL of branched polyethyleneimine (1 mg/mL). After 48 hours of incubation, cells were harvested by centrifugation at 3,000 × g for 5 minutes, resuspended in Buffer A, snap-frozen, and stored at -80 °C for further purification.

All purification steps were performed at 4°C to preserve protein activity. Frozen cell suspensions were rapidly thawed in water, lysed by sonication (200 W for ~0.3 hours), and centrifuged at 20,000 × g for 30 minutes at 4°C. The supernatant was filtered through a 0.22 μm syringe filter to obtain soluble material. A His-Trap Ni-NTA 6FF chromatography column was equilibrated with five column volumes of Buffer A (Buffer A: 50 mM Tris-HCl, pH 8.0, 1000 mM NaCl). The clarified extract was loaded onto the column, washed with Buffer A to remove non-specific proteins, and eluted with a linear gradient of nickel elution buffer (Buffer B: 50 mM Tris-HCl, pH 8.0, 1 M NaCl, 300 mM imidazole, 1 mM DTT). Eluted fractions were analyzed by SDS-PAGE and Coomassie staining. The protein of interest was concentrated, exchanged into Buffer C (50 mM Tris-HCl, pH 8.0, 1000 mM NaCl, 1 mM EDTA, 1

mM DTT) using an Amicon Ultra centrifugal filter unit, following overnight treatment with Benzonase nuclease to eliminate nucleic acid contamination or HRV 3C Protease to cut His-tag. The purification process was subsequently refined through gel filtration using a Superdex 6 Increase column (GE Healthcare) for the MORC2FL. Following this, fragments were conjugated with a GPGS linker, and the resulting mixture was subjected to a size-exclusion chromatography process (Superdex 200/75 column, GE Healthcare) to yield a final solution comprising 50 mM Tris-HCl, pH 8.0, 500 mM NaCl, 1 mM EDTA, and 1 mM DTT. Peak fractions were analyzed by SDS-PAGE and Coomassie staining, confirming the successful purification of highly homogeneous MORC2FL (1-1032) and various fragments (Fig. S7), then flash-frozen in liquid nitrogen and stored at -80°C.

Crystallization, data collection and processing

The CC3 domain (901-1003) and various mutations of MORC2constructs were cloned into a modified pET32M vector (with Trx-tag) using standard PCR-based methods and confirmed by DNA sequencing. Due to the lack of homologous structures, protein crystals with heavy atom derivatives are required to determine their phases. Therefore, we used the methionine-deficient strain B834 to express the target protein with selenomethionine (SeMet) in an inorganic selenosubstituted medium. Recombinant proteins were expressed in *E. coli* B834 cells in M9 medium at 16°C. MORC2 CC3 fused with a GPGS linker were finally changed by step of size-exclusion chromatography (Superdex 75 increase column, GE Healthcare) into 50 mM Tris-HCl, pH 8.0, 100 mM NaCl, 1 mM EDTA and 1 mM DTT). The freshly purified protein was concentrated to 10~20 mg/mL. Crystals were obtained by the static sitting drop method in 0.1M Citric acid (pH 3.5) and 25% w/v PEG 3350 at 25°C. Glycerol (20%) was added as the cryo-protectant. A 3.1-Å resolution X-ray dataset was collected at the beamline BL18U1 of the Shanghai Synchrotron Radiation Facility (SSRF). The diffraction data were processed and scaled by HKL2000 (http://www.hkl-xray.com/). Using the structure of auto-build model by SAD data and AlpahFold2 predicted model as the search model, the initial structural model was

solved by molecular replacement in PHASER (https://www.ccp4.ac.uk/). Further manual model adjustment and refinement were completed iteratively using COOT and PHENIX. The final structure was validated by PISA and MolProbity (https://www.phenix-online.org/). The final refinement statistics of the complex structure are listed in Supplementary Table 1. All structure figures were prepared using the programme PyMOL (http://pymol.sourceforge.net/).

Protein labeling with fluorophore

The Cy3 NHS ester (AAT Bioquest) fluorophores were dissolved in DMSO at 10 mg/mL. Purified proteins were prepared in reaction buffer at a concentration of 10 mg/mL. The fluorophores were added to the protein solution at a 1:1 molar ratio. The reaction was conducted with shaking at room temperature for 1 hour in the dark. After the reaction, labeling was quenched with 200 mM Tris-HCl, pH 8.3, and the labeled proteins were desalted using a HiTrap desalting column (GE Healthcare). Fluorescence labeling efficiency was assessed using a Nanodrop 2000 spectrophotometer (ThermoFisher #ND-2000). The final labeling efficiency of each protein was adjusted to 1% by mixing the labeled protein with an excess of unlabeled protein (1:99 ratio).

Lentiviral mediated H2A-mCherry inducible expression in HeLa cells

Stable expression of H2A-mCherry in HeLa cells was achieved through lentiviral-mediated transduction. First, H2A-mCherry gene sequence was inserted into the inducible lentiviral vector pTRIPZ to generate the expression plasmid pTRIPZ-H2A-mCherry. Lentiviral particles were generated by triple transfection of HEK293T cells with pTRIPZ-H2A-mCherry, PMD2.G, and PSPAX2 plasmids using Lipofectamine 3000. The viral supernatant was collected 48 hours after transfection, filtered with 0.45-μm filter to remove cell debris, and used to transduce HeLa cells. Following transduction, HeLa cells were selected with 50 μg/mL hygromycin to establish stable cell lines. H2A-mCherry expression was induced with 1 μg/mL doxycycline.

Live cell imaging and immunofluorescence staining

For live-cell imaging, HeLa cells were seeded onto 35 mm culture dishes with glass-bottom plates (Biosharp) and transfected with EGFP-MORC2 or its mutant constructs. Images were captured 12 hours post-transfection using a Nikon confocal microscope equipped with an incubator system (37°C, 5% CO_2). Nuclei were stained with Hoechst 33342 or visualized using mCherry-labeled H2A fusion protein. For immunofluorescence, cells were fixed with 4% paraformaldehyde, permeabilized with 0.1% Triton X-100, and blocked with 10% goat serum. Primary antibodies were incubated overnight at 4°C, followed by incubation with fluorescence-conjugated secondary antibodies for 2 hours at room temperature in the dark. Fluorescence images were acquired using a Nikon confocal microscope.

CRISPR-Cas9 mediated MORC2 knockout cells

MORC2 knockout (KO) HeLa cell lines were generated using the CRISPR-Cas9 system. A CRISPR single-guide RNA (sgRNA) targeting exon 5 of MORC2 (5′-ACACCTGAGTCTACTCAGAT-3′) was designed using the online tool (http://crispor.tefor.net/). Two DNA oligos with complementary sgRNA targeting sequence and additional bases were designed as previously described[49,50]. These oligos were annealed and cloned into pLentiCRISPR v2 (Addgene plasmid #52961) to generate the MORC2 knockout vector. After transfection and puromycin selection, MORC2-deleted cells were obtained. Individual cells were sorted into separate wells of a culture plate to establish monoclonal cell lines using flow cytometry. To validate the knockout cell lines, genomic DNA was extracted from both WT and KO cells. The specific regions targeted by the sgRNA were amplified using PCR with primers: 5′-CAACATTCTCGAGCTGGACCTACAG-3′ (forward) and 5′-CCACGACAAGACTGGAAACGTGACTC-3′ (reverse). The PCR products were purified and subjected to Sanger sequencing, revealing the deletion and insertion mutations in the target sites of the MORC2 allelic genes (Fig. S2d).

Generation of endogenous EGFP-MORC2 chimeric mice

CRISPR-Cas9 was used to generate EGFP-MORC2 chimeric mice. The EGFP and linker sequence were inserted at the N-terminus of the mouse *MORC2a* gene. Briefly, a single-guide RNA (sgRNA) was designed to target exon 1 of *MORC2a*, with the sequence GACTGAAGACTCATTGCTGTCA. A donor DNA fragments containing the EGFP-linker region flanked by homologous arms was constructed. Fertilized mouse zygotes were collected, and a mixture of Cas9 mRNA (50 ng/μL), sgRNA (25 ng/μL), and donor DNA (50 ng/μL) was microinjected into pronucleus of the zygotes. The injected embryos were transferred into the oviducts of pseudopregnant recipient female mice. Resulting pups were genotyped by PCR and Sanger sequencing to confirm transgene integration (Fig. S2f). The genotyping primers for the EGFP-MORC2 allele were as follows: Left-F1: GCGGTGGTTGAGTTCCAATTCC; Left-R1: CTTCAGGGTCAGCTTGCCGTAG; Right-F1: GAACGGCATCAAGGTGAACTTC; Right-R1: TGTATCCAAGGTAATCTCTGTGGTA.

Mice were bred at the Animal Center of the University of Science and Technology of China (USTC). Animals were housed under controlled conditions (22 °C, 12-hour light/dark cycle) with free access to food and water ad libitum. All experimental procedures were approved by the Institutional Animal Care and Use Committee (IACUC) of the University of Science and Technology of China (Hefei, China).

Fluorescence recovery after photobleaching (FRAP)

The FRAP assay was performed to investigate the dynamics of protein mobility within condensates, either in *in vivo* or *in vitro*. Specific regions of interest (ROIs) approximately 2 μm² in size were selected and subjected to photobleaching using 100% laser power (488 nm) for approximately 20 ns. One droplet was left unbleached as a control. Fluorescence recovery within the ROI was monitored for 100-300 seconds. FRAP was performed using a 63x oil immersion objective mounted on a Nikon confocal microscope (in cells) or a Zeiss LSM 880 (*in vitro*). Fluorescence intensity

was normalized to the pre-bleach signal to analyze the recovery kinetics. For brain slice FRAP, organotypic brain slices were prepared from adult chimeric mice expressing endogenous EGFP-MORC2, following a slightly modified protocol previously described[49]. After decapitation, brains were rapidly extracted and placed in ice-cold dissection medium consisting of Hibernate A, 2% B27 supplement, 2 mM L-glutamine, and 1% penicillin–streptomycin. The cerebellum and midbrain were removed, and the remaining cerebral hemispheres were coronally sectioned at 250 μm using a McIlwain tissue chopper. Slices were gently separated in chilled dissection medium and transferred onto glass-bottom dishes containing culture medium composed of Neurobasal A, 2% B27 supplement, 2 mM L-glutamine, and 1% penicillin–streptomycin. Imaging was initiated immediately after brain slice preparation. FRAP experiments were performed using the Nikon confocal microscope. Photobleaching was carried out with 5-7 laser pulses (50 μs dwell time), and images were acquired at 2-s intervals. Post-bleach images were acquired 20 s after photobleaching.

Sedimentation assay

To assess concentration-dependent partitioning behavior, purified proteins at the indicated concentrations were incubated under the same buffer conditions used for *in vitro* phase separation assays and equilibrated for 10 min at room temperature. Samples were then centrifuged at 16,000 × g for 10 min to separate the supernatant and pellet fractions. Following centrifugation, the supernatant was carefully collected, and the pellet was resuspended in an equal volume of buffer. Equal volumes of supernatant and pellet fractions were analyzed by SDS–PAGE and quantified by densitometry.

Electrophoretic mobility shift assays (EMSA)

Widom 601 DNA (147 bp, 25 nM) was amplified by PCR and incubated with increasing concentrations of MORC2 or its domain constructs in binding buffer (20 mM Tris-HCl, pH 7.5, 45 mM KCl, 4 mM $MgCl_2$, 5% glycerol, 5 mM DTT). The

reaction mixture was loaded onto a 6% polyacrylamide gel and electrophoresed at 120 V for 70 minutes. DNA was visualized using SYBR Gold stain, and images were captured using the ChemiDoc MP Imaging System.

Size-exclusion chromatography coupled with static light scattering

The analysis was performed using an AKTA FPLC system (GE Healthcare) coupled to a static light scattering detector (miniDawn, Wyatt) and a differential refractive index detector (Optilab, Wyatt). Protein samples (70 μM) were filtered and applied to a Superdex 200 increase or Superose 6 increase column, pre-equilibrated with a column buffer containing 50 mM Tris-HCl, pH 8.0, 150 mM NaCl or 1000 mM NaCl (MORC2FL), 1 mM EDTA, and 1 mM DTT. Data were analyzed using ASTRA6 software (Wyatt).

***In vitro* phase separation and fluorescence microscopy imaging**

Droplet formation was monitored using differential interference contrast (DIC) and fluorescence microscopy. To induce phase separation, protein was added to phase separation buffer (50 mM Tris-HCl, pH 8.0, 150 mM NaCl, 1 mM DTT). For consistency, all MORC2 samples were diluted to a final concentration of 4 μM with phase separation buffer containing 200 mM NaCl, unless otherwise specified. All preparation steps were performed at 4 °C to preserve protein activity. The phase separation mixtures were then equilibrated at room temperature for 20 min. A 5-10 μL aliquot of each sample was placed onto a custom-made glass slide, covered with an 18 mm diameter coverslip, and incubated at room temperature for 20 min before imaging.

Protein isotope labeling and NMR Spectroscopy

Isotopically labeled protein samples were expressed in minimal M9/H_2O or M9/D_2O medium. Uniformly ^{15}N-labeled (or ^{13}C- or ^{15}N-labeled) protein samples were prepared in M9/H_2O medium supplemented with 1 g/L of $^{15}NH_4Cl$ and 2 g/L of glucose (or ^{13}C-glucose). The cells were harvested at an OD_{600} of approximately

1.0. Isotope-labeled precursors and amino acids were purchased from Cambridge Isotope Laboratories (CIL). Isotopically labeled samples were prepared in 50 mM Tris-HCl, pH 8.0, 100 mM NaCl, and 7% D O. Protein concentrations ranged from 0.5 to 1.0 mM. NMR experiments were performed using Bruker Avance III 600 MHz spectrometers equipped with a cryo-probe. NMR spectra of MORC2 and its complex were recorded at 298 K. Backbone assignments of MORC2$^{1004\text{-}1032}$ were obtained using SOFAST versions of standard triple-resonance experiments, including HNCACB and CBCACONH, recorded at 298 K. Residual assignment ambiguities were resolved using ^{15}N-edited HMQC-NOESY-HMQC spectra. All NMR spectra were processed using NMRPipe and analyzed with NMRViewJ software (http://www.onemoonscientific.com). CSPs were calculated in Hz at 600 MHz using the following equation:

$$\Delta v = ((\Delta^{1}\mathrm{H} \times 600)^{2} + (\Delta^{13}\mathrm{C} \times 150)^{2})^{1/2}$$

Fluorescence polarization Assay (FP)

Fluorescence polarization (FP) assays were performed at room temperature (25 °C) using a BioTek H1 fluorescence spectrophotometer to evaluate the binding affinity between MORC2 protein and 5-carboxyfluorescein (5-FAM)-labeled 601 DNA (FAM-601) across a concentration range of 0-2000 nM. The 147-bp Widom 601 DNA fragment was generated via PCR amplification using a 5-FAM-labeled primer. The labeled primer was dissolved in 0.1 M NaHCO buffer, pH 8.3, and the amplified product was purified by agarose gel extraction to eliminate residual primers and nonspecific amplification products.

Fluorescence measurements were carried out in assay buffer (50 mM Tris-HCl, pH 8.0, 150 mM NaCl, 1 mM EDTA, 1 mM DTT, and 10% glycerol) containing purified FAM-601 DNA at a final concentration of 0.4 ng/μL. Excitation and emission wavelengths were optimized according to the instrument manual, with excitation set at 485 nm and emission at 525 nm. Fluorescence polarization values were recorded in triplicate, and control measurements were included to correct for background signals.

Data were analyzed to determine the equilibrium dissociation constant (K_d) for the MORC2-FAM-601 interaction by fitting data to a log(agonist) vs. response model. In parallel, the effect of small molecules on this binding interaction was assessed by introducing compounds into the assay mixture and monitoring changes in fluorescence polarization.

ATPase activity measurements

ATPase activity was measured[52] using 1 μM MORC2 or its mutant variants at 37°C in 50 mM Tris-HCl, pH 8.0, 150 mM NaCl, 8 mM $MgCl_2$, 10% glycerol and 5 mM ATP. All experiments were repeated independently at least three times.

RNA-seq and bioinformatic analysis

MORC2-knockout HeLa cells were seeded at equal density and transfected with 3 μg of plasmid DNA and 12 μg of PEI (polyethylenimine) per dish. After 6 hours, the transfection medium was replaced with fresh complete medium, and cells were incubated for an additional 48 hours. Cells were then washed twice with ice-cold PBS and lysed directly in RNA Isolator (R401, Vazyme) on ice. Total RNA was extracted using the RNeasy Mini Kit (Qiagen, 74004) according to the manufacturer's protocol. RNA quality was assessed using NanoDrop 2000 (Thermo Fisher Scientific), Agilent 2100 Bioanalyzer, and LabChip GX (PerkinElmer). For library preparation, 1 μg of total RNA was used per sample, employing the VAHTS Universal V6 RNA-seq Library Prep Kit for MGI®. The resulting double-stranded DNA libraries were denatured, circularized, and digested to obtain single-stranded circular DNA. DNA nanoballs (DNBs) were generated from these templates through rolling circle amplification (RCA). Sequencing was performed on the MGI DNBSEQ-T7 platform (MGI Tech Co., Ltd) using combinatorial Probe-Anchor Synthesis (cPAS) chemistry.

Before performing differential expression analysis, lowly expressed genes were filtered out by retaining only those with a raw count of ≥10 in at least three samples (baseMean). Differential gene expression analysis between sample groups was carried

out using the DESeq2 package (v1.26.0). Genes with *p-adjust* < 0.05 were defined as differentially expressed genes (DEGs). These DEGs were subsequently subjected to Gene Ontology (GO) enrichment analysis in DAVID (Knowledgebase v2025_1).

Statistical Analysis

All statistical analyses were performed in GraphPad Prism. All data underwent normality testing (D'Agostino & Pearson test and Anderson-Darling test) in advance. Two-tailed unpaired Student's *t*-test post-hoc Welch's correction and one-way ANOVA with Tukey's post hoc test was used when data were distributed normally. The significance level was set as $p < 0.05$. All statistical results are provided as Source Data.

Acknowledgments

We thank Dr. Xuebiao Yao (University of Science and Technology of China, USTC), Dr. Zhi Qi and Dr. Linyu Zuo (Peking University) for helpful discussion. We thank members of the Shanghai Synchrotron Radiation Facility (SSRF, China; beamlines BL02U1, BL18U1, and BL19U1) for X-ray beam time. This work was supported by grants from the National Key R&D Program of China (2019YFA0508402), the National Natural Science Foundation of China (22122703, 32470808, 32170767, 32471273, 31971144, and T2221005), the Center for Advanced Interdisciplinary Science and Biomedicine of IHM (QYPY20220014), the Strategic Priority Research Program of the Chinese Academy of Sciences (XDB0490000), the Major Frontier Research Project of USTC (LS9100000002), USTC Research Funds of Double First-Class Initiative (YD9100002507 and YD9100002054), the Anhui Medical University Foundation (9101224201), and National Natural Science Foundation Incubation Program of The Second Affiliated Hospital of Anhui Medical University (2021GQFY02).

Author contributions

Y.Z., W.X., W.D., C.H., C.W., and Y.B. designed the experiments. Y.B., Y.Z., W.X., and W.D. conducted the experiments. Y.Z. determined the crystal structure. Y.W., W.J. and F.Z. assisted with the experiments and reagents. All authors analyzed the data. Y.Z., Y.B., C.H., and C.W. wrote the manuscript with input from all authors. All authors approved the final version of the manuscript. C.H., and C.W supervised the project.

Competing interests

The authors declare that they have no competing interests.

Data and materials availability

All data needed to evaluate the conclusions in the paper are present in the paper and/or the Supplementary Materials. Raw gene expression data are available in Source Data. The atomic coordinates of the MORC2 CC3 domain have been deposited to the Protein Data Bank under the accession code: 9KQL.

References

1. Alabert, C. & Groth, A. Chromatin replication and epigenome maintenance. *Nat Rev Mol Cell Biol* **13**, 153–167 (2012).
2. Ishihara, S. *et al.* Local states of chromatin compaction at transcription start sites control transcription levels. *Nucleic Acids Res* **49**, 8007–8023 (2021).
3. Downs, J. A. & Gasser, S. M. Chromatin remodeling and spatial concerns in DNA double-strand break repair. *Curr Opin Cell Biol* **90**, 102405 (2024).
4. Blackledge, N. P. & Klose, R. J. The molecular principles of gene regulation by Polycomb repressive complexes. *Nat Rev Mol Cell Biol* **22**, 815–833 (2021).
5. Li, D.-Q. *et al.* MORC2 signaling integrates phosphorylation-dependent, ATPase-coupled chromatin remodeling during the DNA damage response. *Cell Rep* **2**, 1657–1669 (2012).
6. Müller, I. & Helin, K. Keep quiet: the HUSH complex in transcriptional silencing and disease. *Nat Struct Mol Biol* **31**, 11–22 (2024).
7. Zhong, Z. *et al.* MORC proteins regulate transcription factor binding by mediating chromatin compaction in active chromatin regions. *Genome Biol* **24**, 96 (2023).
8. Xue, Y. *et al.* Arabidopsis MORC proteins function in the efficient establishment of RNA directed DNA methylation. *Nat Commun* **12**, 4292 (2021).
9. Weiser, N. E. *et al.* MORC-1 Integrates Nuclear RNAi and Transgenerational Chromatin Architecture to Promote Germline Immortality. *Developmental Cell* **41**, 408-423.e7 (2017).
10. Moissiard, G. *et al.* MORC family ATPases required for heterochromatin condensation and gene silencing. *Science* **336**, 1448–1451 (2012).
11. Wang, H., Zhang, L., Luo, Q., Liu, J. & Wang, G. MORC protein family-related signature within human disease and cancer. *Cell Death Dis* **12**, 1112 (2021).
12. Tchasovnikarova, I. A. *et al.* Hyperactivation of HUSH complex function by Charcot-Marie-Tooth disease mutation in MORC2. *Nature Genetics* (2017) doi:10.1038/ng.3878.
13. Douse, C. H. *et al.* Neuropathic MORC2 mutations perturb GHKL ATPase dimerization dynamics and epigenetic silencing by multiple structural mechanisms. *Nat Commun* **9**, 651 (2018).
14. Xie, H.-Y., Zhang, T.-M., Hu, S.-Y., Shao, Z.-M. & Li, D.-Q. Dimerization of MORC2 through its C-terminal coiled-coil domain enhances chromatin dynamics and promotes DNA repair. *Cell Commun Signal* **17**, 160 (2019).
15. Morais Cabral, J. H. *et al.* Crystal structure of the breakage-reunion domain of DNA gyrase. *Nature* **388**, 903–906 (1997).
16. Chen, K. *et al.* Crystal structure of the hinge domain of Smchd1 reveals its dimerization mode and nucleic acid-binding residues. *Sci Signal* **13**, eaaz5599 (2020).
17. Liu, J. *et al.* Cascading MutS and MutL sliding clamps control DNA diffusion to activate mismatch repair. *Nature* **539**, 583–587 (2016).
18. Ortega, J., Lee, G. S., Gu, L., Yang, W. & Li, G.-M. Mispair-bound human MutS-MutL complex triggers DNA incisions and activates mismatch repair. *Cell Res* **31**, 542–553 (2021).
19. Lee, K. *et al.* The structure of an Hsp90-immunophilin complex reveals cochaperone recognition of the client maturation state. *Mol Cell* **81**, 3496-3508.e5 (2021).
20. Pastor, W. A. *et al.* MORC1 represses transposable elements in the mouse male germline. *Nat Commun* **5**, 5795 (2014).
21. Dopkins, N. *et al.* A field guide to endogenous retrovirus regulatory networks. *Mol Cell* **82**,

3763–3768 (2022).
22. Fendler, N. L. *et al.* Identification and characterization of a human MORC2 DNA binding region that is required for gene silencing. *Nucleic Acids Res* **53**, gkae1273 (2025).
23. Leidescher, S. *et al.* Spatial organization of transcribed eukaryotic genes. *Nat Cell Biol* **24**, 327–339 (2022).
24. Membrane-less compartments in the nucleus: Separated or connected phases? *Current Opinion in Cell Biology* **84**, 102215 (2023).
25. Boeynaems, S. *et al.* Protein Phase Separation: A New Phase in Cell Biology. *Trends Cell Biol* **28**, 420–435 (2018).
26. Yoshizawa, T. *et al.* Nuclear Import Receptor Inhibits Phase Separation of FUS through Binding to Multiple Sites. *Cell* **173**, 693-705.e22 (2018).
27. Verba, K. A. *et al.* Atomic structure of Hsp90-Cdc37-Cdk4 reveals that Hsp90 traps and stabilizes an unfolded kinase. *Science* **352**, 1542–1547 (2016).
28. Alberti, S., Gladfelter, A. & Mittag, T. Considerations and Challenges in Studying Liquid-Liquid Phase Separation and Biomolecular Condensates. *Cell* **176**, 419–434 (2019).
29. Zhang, Y. *et al.* MORC3 Forms Nuclear Condensates through Phase Separation. *iScience* **17**, 182–189 (2019).
30. Kalderon, D., Roberts, B. L., Richardson, W. D. & Smith, A. E. A short amino acid sequence able to specify nuclear location. *Cell* **39**, 499–509 (1984).
31. Alderson, T. R. & Kay, L. E. NMR spectroscopy captures the essential role of dynamics in regulating biomolecular function. *Cell* **184**, 577–595 (2021).
32. Kim, T. H. *et al.* Phospho-dependent phase separation of FMRP and CAPRIN1 recapitulates regulation of translation and deadenylation. *Science* **365**, 825–829 (2019).
33. Murthy, A. C. *et al.* Molecular interactions underlying liquid−liquid phase separation of the FUS low-complexity domain. *Nat Struct Mol Biol* **26**, 637–648 (2019).
34. Zhang, Y., Stöppelkamp, I., Fernandez-Pernas, P. et al. Probing condensate microenvironments with a micropeptide killswitch. *Nature* **643**, 1107–1116 (2025).
35. Pandiloski, N. *et al.* DNA methylation governs the sensitivity of repeats to restriction by the HUSH-MORC2 corepressor. *Nat Commun* **15**, 7534 (2024).
36. Fukuda, K., Okuda, A., Yusa, K. & Shinkai, Y. A CRISPR knockout screen identifies SETDB1-target retroelement silencing factors in embryonic stem cells. *Genome Res* **28**, 846–858 (2018).
37. Liu, N. *et al.* Selective silencing of euchromatic L1s revealed by genome-wide screens for L1regulators. *Nature* **553**, 228–232 (2018).
38. Jacquier, A., Roubille, S., Lomonte, P. & Schaeffer, L. Microrchidia CW-Type Zinc Finger 2, a Chromatin Modifier in a Spectrum of Peripheral Neuropathies. *Front Cell Neurosci* **16**, 896854 (2022).
39. Stafki, S. A. *et al.* The Spectrum of MORC2-Related Disorders: A Potential Link to Cockayne Syndrome. *Pediatr Neurol* **141**, 79–86 (2023).
40. Chung, H. Y. *et al.* Morc2a variants cause hydroxyl radical-mediated neuropathy and are rescued by restoring GHKL ATPase. *Brain* **147**, 2114–2127 (2024).
41. Ding, Q.-S. *et al.* Aberrant high expression level of MORC2 is a common character in multiple cancers. *Hum Pathol* **76**, 58–67 (2018).
42. Zhang, S. *et al.* Oncogenic MORC2 in cancer development and beyond. *Genes Dis* **11**, 861–873

(2024).
43. Li, D.-Q., Nair, S. S. & Kumar, R. The MORC family: new epigenetic regulators of transcription and DNA damage response. *Epigenetics* **8**, 685–693 (2013).
44. Koch, A. *et al*. MORC Proteins: Novel Players in Plant and Animal Health. *Front Plant Sci* **8**, 1720 (2017).
45. Dong, W. *et al*. MORC Domain Definition and Evolutionary Analysis of the MORC Gene Family in Green Plants. *Genome Biol Evol* **10**, 1730–1744 (2018).
46. Inoue, N. *et al*. New gene family defined by MORC, a nuclear protein required for mouse spermatogenesis. *Hum Mol Genet* **8**, 1201–1207 (1999).
47. Wang, G.-L. *et al.* Identification and expression analysis of a novel CW-type zinc finger protein MORC2 in cancer cells. *Anat Rec (Hoboken)* **293**, 1002–1009 (2010).
48. Tan, W., Park, J., Venugopal, H. et al. MORC2 is a phosphorylation-dependent DNA compaction machine. Nat Commun 16, 5606 (2025).
49. Shalem, O. *et al.* Genome-scale CRISPR-Cas9 knockout screening in human cells. *Science* **343**, 84–87 (2014).
50. Sanjana, N. E., Shalem, O. & Zhang, F. Improved vectors and genome-wide libraries for CRISPR screening. *Nat Methods* **11**, 783–784 (2014).
51. Li, C. H. *et al.* MeCP2 links heterochromatin condensates and neurodevelopmental disease. *Nature* **586**, 440–444 (2020).
52. Microtiter assay for glutamine synthetase biosynthetic activity using inorganic phosphate detection. *Analytical Biochemistry* **327**, 114–118 (2004).

Table S1

Statistics of X-ray Crystallographic Data Collection and Model refinement

Data collection	
Data sets	MORC2-CC3
Space group	*I41*
Wavelength (Å)	0.97915
Unit Cell Parameters (Å)	a=130.253, b=130.253, c= 40.895 α=β=γ=90°
Resolution range (Å)	50-3.05 (3.10-3.05)
No. of unique reflections	6774 (333)
Redundancy	12.6 (10.5)
I/σ	25.897 (2.600)
Completeness (%)	100.0 (100.0)
R_{merge} [a] (%)	12.0 (121.4)
$CC_{1/2}$ (last resolution shell) [b]	0.703
Structure refinement	
Resolution (Å)	32.56-3.10
R_{cryst} [c]/R_{free} [d] (%)	19.81 / 24.80
Rmsd bonds (Å) / angles (°)	0.004 / 0.627
Average B factor ($Å^2$) [e]	57.55
No. of atoms	
Protein atoms	1543
Water	6
Ligands	0
Ramachandran plot regions [e]	
Favored (%)	98.99
Allowed (%)	1.01
Outliers (%)	0

Numbers in parentheses represent the value for the highest resolution shell.

(**a**) $R_{merge} = \Sigma\ |I_i - \ | \ / \ \Sigma I_i$, *where* I_i *is the intensity of measured reflection and is the mean intensity of all symmetry-related reflections.*

(b) *$CC_{1/2}$ were defined by Karplus and Diederichs.*

(c) *$R_{cryst}=\Sigma||F_{calc}| - |F_{obs}||/\Sigma F_{obs}$, where F_{obs} and F_{calc} are observed and calculated structure factors.*

(d) *$R_{free}= \Sigma_T||F_{calc}| - |F_{obs}||/\Sigma F_{obs}$, where T is a test data set of about 5% of the total unique reflections randomly chosen and set aside prior to refinement.*

(e) *B factors and Ramachandran plot statistics are calculated using MOLPROBITY.*

Table S2. *Summary of MORC2 protein constructs used in this study, including expression systems, extinction coefficients, A260/280 ratios, and corresponding experimental applications.*

MORC2 fragment in vitro	***Expression system***	***Ext. coefficient***	***A260/280 ratios***	***Experimental applications***
MORC2FL (1-1032)	***E. coli***	*88240*	*0.59*	*EMSA, Agarose gel analysis (AGA)*
CTD (473-1032)	*E. coli*	*46410*	*0.71*	*EMSA; Phase separation*
CTD∆CW (537-1032)	*E. coli*	*26930*	*0.58*	*EMSA; Phase separation; FPLC-MALS*
TCD-CC3-IBD (744-1032)	*E. coli*	*26930*	*0.67*	*EMSA; FPLC-MALS*
CC3-IBD (901-1032)	*E. coli*	*7450*	*0.51*	*EMSA; FPLC-MALS, AGA*
CC1 (279-362)	*E. coli*	*1490*	*0.53*	*EMSA*
CC2 (551-603)	*E. coli*	*0*	*ND*	*EMSA*
CC3 (901-1003)	*E. coli*	*5960*	*0.49*	*FPLC-MALS NMR; Structure determination, AGA*
IDR (593-735)	*E. coli*	*0*	*ND*	*EMSA*
IBD (1004-1032)	*E. coli*	*1490*	*0.58*	*NMR*
IDRa (593-643)	*E. coli*	*0*	*ND*	*NMR*
IDRb (644-694)	*E. coli*	*0*	*ND*	*NMR*
IDRc (695-735)	*E. coli*	*0*	*ND*	*NMR*
Trx-CC3	*E. coli*	*21555*	*0.6*	*FPLC-MALS*
Trx-CC3^{trun}_901-975	*E. coli*	*14105*	*0.58*	*FPLC-MALS*
Trx-CC3-IBD_L915Q	*E. coli*	*21555*	*0.91*	*FPLC-MALS*
Trx-CC3-IBD_F922Q	*E. coli*	*21555*	*0.59*	*FPLC-MALS*
Trx-CC3-IBD_L911Q	*E. coli*	*21555*	*0.6*	*FPLC-MALS*
Trx-CC3-IBD_I908Q	*E. coli*	*21555*	*0.6*	*FPLC-MALS*
Trx-CC3-IBD_F951Q	*E. coli*	*21555*	*0.54*	*FPLC-MALS*
Trx-CC3-IBD_Y921A	*E. coli*	*20065*	*0.56*	*FPLC-MALS*
Trx-CC3-IBD_F954Q	*E. coli*	*21555*	*0.53*	*FPLC-MALS*
Trx-CC3-IBD_L958Q	*E. coli*	*21555*	*0.58*	*FPLC-MALS*
MORC2FL (1-1032)	***HEK293F***	*88240*	*0.6*	*FPLC-MALS; Phase separation; FP; ATPase activity, AGA*
MORC2∆CC3-IBD (1-900)	*HEK293F*	*80790*	*0.56*	*FPLC-MALS*
MORC2_N39A	*HEK293F*	*88240*	*0.79*	*FP; ATPase activity*
MORC2_R252W	*HEK293F*	*93740*	*0.66*	*FP; ATPase activity*
MORC2_Q400R	*HEK293F*	*88240*	*0.65*	*FP; ATPase activity*
MORC2_D466N	*HEK293F*	*88240*	*0.58*	*FP; ATPase activity*
MORC2_S87L	*HEK293F*	*88240*	*0.75*	*FP; ATPase activity*

MORC2_S218L	*HEK293F*	*88240*	*0.72*	*FP; ATPase activity*
MORC2_F256L	*HEK293F*	*88240*	*0.6*	*FP; ATPase activity*
MORC2_R266A	*HEK293F*	*88240*	*0.75*	*FP; ATPase activity*
MORC2_T424R	*HEK293F*	*88240*	*0.55*	*FP; ATPase activity*
EGFP-MORC2FL	*HEK293F*	*110130*	*0.59*	*Phase separation; FRAP, AGA*

Figure Legend

Fig. 1 The CC3 domain serves as the structural basis for full-length MORC2 dimerization.

*(**a**) The domain organization of human MORC2FL, highlighting the ATPase module (GHL, CC1 and S5 domains, collectively termed NTD), the C-terminal domains (CTD) with coiled-coil regions (CC2 and CC3), CW-type zinc finger (CW), intrinsically disordered region (IDR, marked by a fresh green line by IUPRED2 prediction), nuclear localization signal (NLS), Tudor-chromodomain (TCD), and a 30-residues tail domain (IBD).*

*(**b**) Purification and characterization of full-length human MORC2 in HEK293F cell system. SDS-PAGE analysis of the purified protein demonstrates its purity and distribution.*

*(**c**) Static light-scattering (SLS) analysis shows that MORC2 forms dimers in the absence of ATP, with a molecular weight of 239 ± 1 kDa in standard buffer (mint green line) and 303 ± 2 kDa in the presence of 601 DNA (sunflower yellow line).*

*(**d**) SLS analysis reveals the oligomerization states of MORC2 truncations. Full-length MORC2 lacking CC3-IBD (1-900) is monomeric, while CC3-IBD (901-1032) and CC3 alone (901-1003) form stable dimers.*

*(**e**) Crystal structural of the CC3 dimer. Hydrophobic residues contributing to dimer stability (L911, L915, and F922) are highlighted using ball-and-stick representations. Top view of the hydrophobic core of the CC3 dimer. Layers of hydrophobic contacts stabilize the dimer interface, illustrated with paired residues (e.g., Layer 1: L911-L911', Layer 2: L915-L915', and Layer 3: F922-F922').*

*(**f**) Additional SLS analysis confirms that fragments spanning residues 537-1032, 744-1032, and Trx-901-975 (CC3 truncation) adopt dimeric conformations.*

Fig. 2 Endogenous MORC2 organizes into dynamic condensates within the nucleus

*(**a**) SDS-PAGE analysis of EGFP-MORC2FL protein purified from HEK293F cells, showing protein concentration at 2.5 μM and 5 μM.*

*(**b**) Sedimentation assay shows the distribution of EGFP-MORC2FL (7.2 μM) between supernatant (S) and pellet (P) fractions under 1000 mM (control) and 150 mM NaCl, indicating its propensity for phase separation.*

*(**c**) EGFP-MORC2 (7.2 μM) undergoes phase separation into droplets in a buffer containing 150 mM NaCl, but not in 1000 mM NaCl buffer. Scaler bar: 2 μm.*

*(**d**) The proteins were examined in a buffer containing 150 mM NaCl, and phase separation was assessed by fluorescence microscopy with 488 nm excitation for EGFP. Quantification of droplet areas from (**Fig. S2a**), presented as violin plots with box plots indicating medians. Data are derived from ≥ 3 independent images and reflect the size distribution of phase-separated droplets. Data are presented as mean ± SEM; one-way ANOVA with Tukey's post hoc test. ****$p < 0.0001$; *$p < 0.05$.*

*(**e**) Time-lapse FRAP imaging of EGFP-MORC2FL droplets formed in vitro, demonstrating fluorescence recovery over time. Scaler bar: 2 μm.*

*(**f**) Quantitative analysis of fluorescence recovery from (**e**), showing the dynamic properties of in vitro MORC2 droplets. Data represent mean ± SEM, with n ≥ 3 replicates.*

*(**g**) Immunostaining of endogenous MORC2 in HeLa cells revealed punctate localized within the nucleus, likely representing condensates involved in transcriptional regulation (white arrows). Nuclei are counterstained with DAPI to visualize chromatin-rich regions. Scaler bar: 5 μm.*

*(**h**) Live-cell imaging of transiently transfected EGFP-MORC2FL showed its assembly into dispersed,*

nearly spherical condensates in the nucleus, while stable expression of H2A-mCherry served to mark chromatin-enriched domains. Scaler bar: 10 μm.

***(i)** Time-lapse FRAP analysis of EGFP-MORC2FL condensates in the nuclei of transiently transfected HeLa cells revealed rapid fluorescence recovery within seconds, indicative of their dynamic, nature. Scaler bar: 1 μm.*

***(j)** Quantitative analysis of fluorescence recovery from **(i)**, showing the dynamic properties of in vitro MORC2 droplets. Data represent mean ± SEM, with n ≥ 10 replicates.*

***(k)** Sections of brain and spinal cord from endogenous EGFP-MORC2 chimeric mice show EGFP-MORC2 condensation distribution in NeuN-positive neurons. Scaler bar: 10 μm.*

***(l)** Representative FRAP images from of FRAP experiments performed on fresh 250-μm brain slices of endogenous EGFP-MORC2 chimeric mice demonstrate the dynamic nature of endogenous MORC2 condensates. Data are presented as mean ± SEM, with n = 3 droplets analyzed. Scaler bar: 5 μm.*

Fig. 3 Multiple domains regulate phase separation of MORC2.

***(a)** Sequential deletion analysis revealed that the NTD is dispensable for condensate formation, as EGFP-tagged NTD alone failed to form condensates and was excluded from the nucleus. Fusion with a canonical nuclear localization signal ("PKKKRKV") restored nuclear localization but did not rescue condensate formation. In contrast, the CTD alone was sufficient to form nuclear condensates. Deletion of the CW domain resulted in enlarged condensates in a subset of cells, while removal of CC2 or the TCD had no apparent effect on condensate formation. Strikingly, deletion of either the IDR or CC3 completely abolished nuclear condensate assembly. Deletion of the IBD markedly reduced the frequency of condensate formation. Loss of the intrinsic NLS led to cytoplasmic localization of MORC2; however, no condensates were detected in the cytoplasm under transient transfection conditions in HeLa cells. Together, these results define the IDR and CC3 as the minimal and essential elements for MORC2-mediated phase separation, and implicate the CW domain, IBD, and nuclear microenvironment in the fine-tuning of condensate assembly. Scaler bar: 10 μm.*

***(b)** In vitro phase separation of Cy3-labeled CTDΔCW at concentrations from 1.25 μM to 20 μM in 150 mM NaCl buffer, visualized as spherical condensates. Scaler bar: 10 μm.*

***(c)** Quantification of droplet areas from (b), displayed as violin plots with box plots indicating median values. Data are presented as mean ± SEM; one-way ANOVA with Tukey's post hoc test. ****p < 0.0001, n.s. not significant.*

***(d)** SDS-PAGE analysis of Cy3-CTDΔCW protein distribution between supernatant (S) and pellet (P) fractions after centrifugation at increasing concentrations (5 μM to 40 μM) in 150 mM NaCl buffer. At 40 μM, increasing the NaCl concentration to 300 mM or 500 mM reduced droplet formation, indicating salt sensitivity.*

***(e)** Quantification of Cy3-CTDΔCW showing the percentage of soluble protein from densitometric analysis of S/P fractions in panel **(d)**, based on three independent biological replicates.*

Fig. 4 Multivalent interactions between IDR and IBD drive MORC2 condensation.

***(a)** Domain organization of MORC2 C-terminal regions analyzed by NMR titration, including the IDR, CC3, and IBD.*

***(b)** ^{15}N-labeled CC3 (residues 901–1003) shows no chemical shift upon titration with IDR (residues 593–735), indicating no detectable interaction.*

***(c)** ^{15}N-labeled IBD (residues 1004–1032) exhibits clear chemical shift perturbations (CSPs) upon IDR*

titration, confirming a direct, specific interaction.

(d-f) *NMR titrations of ^{15}N-labeled IBD with IDR subregions: IDRa (593–643), IDRb (644–694), and IDRc (695–735). IDRa induces clear CSPs* ***(d)****, while IDRb* ***(e)*** *and IDRc* ***(f)*** *show minimal or no shifts, identifying IDRa as the primary IBD-binding segment.*

(g) *Sequence analysis of IDR subregions reveals that IDRa is enriched in proline and arginine residues, enabling electrostatic interactions. Sequence alignment of IBD across species highlights conserved residues involved in IDRa binding. A summary table lists representative residues from IDRa and IBD exhibiting CSPs in titration assays (marked with asterisks).*

(h) *Representative confocal images of HeLa cells expressing EGFP-tagged MORC2ΔIDRa, ΔIDRb, or ΔIDRc constructs. Scale bar: 10 μm.*

(i) *Quantification of droplet area per cell in (h). Deletion of IDRa significantly impairs condensate formation. n = 10 cells per condition. Data are presented as mean ± SEM; statistical analysis: one-way ANOVA with Tukey's post hoc test. ***p < 0.001; n.s. not significant.*

(j) *Working model of MORC2 condensates. CC3 dimerization serves as a structural scaffold, while weak, transient, but specific multivalent interactions between IDRa and IBD cooperatively promote condensate formation.*

Fig. 5 DNA binding enhances MORC2 condensation and modulates its ATPase activity.

(a) *Electrophoretic mobility shift assay (EMSA) showing that MORC2FL binds 25 nM 601 DNA, as evidenced by shifts in DNA mobility corresponding to protein-DNA complexes.*

(b) *EMSA highlighting the strong DNA-binding affinity of the CC1 domain, corroborating previous reports that identify this region as a key mediator of DNA interaction.*

(c-f) *EMSA results demonstrating the binding capacities of individual MORC2 domains to 25 nM 601 DNA: CC2* ***(c)****, IDR* ***(d)****, TCD-CC3-IBD* ***(e)****, and CC3-IBD* ***(f)****. The IDR exhibits robust DNA-binding activity, CC2 and TCD-CC3-IBD show weaker interactions, and CC3-IBD alone fails to bind DNA. These findings identify CC1, CC2, IDR, and the TCD as DNA-binding domains of MORC2.*

(g) *Confocal imaging showing that 601 DNA promotes MORC2 phase separation. At 0.9 μM, EGFP-MORC2FL alone does not form droplets, but the addition of 25 nM 601 DNA induces distinct condensate formation. Scaler bar: 5 μm.*

(h) *Quantification of MORC2 condensate sizes with or without 601 DNA. Violin plots illustrate the distribution of droplet sizes, with box plots indicating median values. Data are presented as mean ± SEM; unpaired student t-test. ****p < 0.0001.*

(i) *Fluorescence microscopy showing Cy3-labeled CTDΔCW (1.25 μM) coalescing with 25 nM FAM-labeled 601 DNA. DNA is recruited into MORC2 droplets, forming distinct condensates. Scaler bar: 5 μm.*

(j) *In the presence of 10 nM 601 DNA, the ATP hydrolysis activity of MORC2FL is significantly enhanced. The N39A mutant, which is deficient in ATP binding, serves as a negative control; nevertheless, a slight but detectable increase in ATPase activity is observed upon DNA binding. ATP hydrolysis activity of MORC2FL is significantly increased in the presence of 10 nM 601 DNA. The N39A mutant, which is deficient in ATP binding, serves as a negative control. Data are presented as mean ± SEM; statistical analysis: one-way ANOVA with Tukey's post hoc test. ****p < 0.0001.*

Fig. 6 Dynamic MORC2 condensation is required for its transcriptional regulatory activity.

(a) *Schematic diagram showing the fusion of two 17–amino acid killswitch sequences to the C terminus*

of MORC2.

(b) *Live-cell FRAP images of HeLa cells overexpressing EGFP–MORC2 full length (FL) and EGFP–MORC2–Killswitch (+KS). Scaler bar: 1 μm.*

(c) *FRAP analysis of EGFP–MORC2 condensates in the nucleus. Data represent mean ± SEM, with n = 11 replicates.*

(d) *Schematic of the rescue experiment strategy. HeLa cells with CRISPR-Cas9-mediated MORC2 knockout were reconstituted with EGFP, EGFP-MORC2FL, or phase separation-deficient mutants EGFP-MORC2ΔCC3 and EGFP-MORC2ΔIDR, and dynamics-defective +KS mutant.*

(e) *RNA-seq-derived read counts for the MORC2 gene in EGFP, EGFP-MORC2FL, EGFP-MORC2ΔCC3, EGFP-MORC2ΔIDR, and EGFP-MORC2FL+KS expressing cells.*

(f) *The effect of MORC2 rescue on the transcriptome. MA plot showing all significantly differentially expressed genes between EGFP–MORC2FL and EGFP transfection in MORC2-knockout HeLa cells (n = 1,074; DESeq2 adjusted $p < 0.05$), highlighted in red.*

(g) *GO-based biological process terms enriched among all differentially expressed genes. Data represent mean ± SD, with n = 3 replicates.*

(h) *Abundance trajectories of all regulated genes, normalized to their respective mean values. Shown is a selected panel of ten downregulated genes that are influenced by MORC2 rescue but show reduced responsiveness to all three mutants.*

(i) *Venn diagram illustrating the overlap between differentially expressed genes identified following EGFP-MORC2FL overexpression in this study and previously characterized MORC2-regulated targets. Fold-change (log□ fold change) analysis of the 84 overlapping genes showing significant expression changes upon MORC2FL overexpression, compared with their corresponding fold changes following overexpression of the three MORC2 mutants. Dashed lines connect the same gene across the four transfection conditions.*

Fig. 7 Pathogenic variants of MORC2 alter condensates behavior, DNA binding, and ATPase activity.

*(**a**) Schematic illustration of pathogenic MORC2 mutations associated with Charcot-Marie-Tooth disease type 2Z (CMT2Z, red) and spinal muscular atrophy (SMA, blue), mapped onto the MORC2 domain structure.*

*(**b**) Quantification of HeLa cells transfected with WT MORC2 or nine pathogenic mutations exhibiting nuclear condensates was performed for each field of view. E236G and T424R shows the most pronounced enhancement of phase separation. n ≥ 10 fields. Data are presented as mean ± SEM; one-way ANOVA with Tukey's post hoc test. ****p□<□0.0001, **p□<□0.01, n.s. not significant.*

*(**c**) ATPase activity of WT MORC2 and eight pathogenic variants, measured under revised conditions. S218L, F256L, and T424R exhibit significantly elevated activity. We were unable to purify MORC2 constructs bearing the E236G mutation from either HEK293F cells, suggesting that it may cause misfolding of the ATPase module. Data are presented as mean ± SEM; one-way ANOVA with Tukey's post hoc test. ****p□<□0.0001, **p□<□0.01, n.s. not significant.*

*(**d**) Fluorescence polarization (FP) analysis of DNA binding affinities to the 601 DNA sequence. All protein variants were evaluated under uniform assay conditions, including those pertinent to phase separation. Dissociation constants (K_d) were determined by fitting the FP data to a log(agonist) vs. response model and are reported as mean ±SEM: WT (98 ± 1 nM), R252W (51 ± 2 nM), Q400R (145 ± 26 nM), D466N (49 ± 6 nM), S87L (107 ± 24 nM), S218L (92 ± 10 nM), F256L (69 ± 2 nM), R266A (63*

± 5 nM), and T424R (242 ± 13 nM). Several variants, including R252W, D466N, F256L, and R266A, demonstrated increased binding affinity relative to WT, while others, such as T424R and Q400R, exhibited markedly reduced binding.

***(e)**. Live-cell FRAP images of HeLa cells overexpressing EGFP–MORC2 full length (FL), E236G, and T424R mutants. Scaler bar: 1 μm.*

***(f)**. FRAP analysis of EGFP–MORC2 condensates in the nucleus. Data represent mean ± SEM, with n ≥ 32 replicates.*

***(g)** A Mechanistic Model of MORC2-Mediated Chromatin Condensation. MORC2 functions as a multivalent DNA-binding machine. The C-terminal CC3-IBD and IDR serve as the structural engine for phase separation, while DNA acts as a scaffold that lowers the phase boundary. The N-terminal ATPase domain undergoes conformational cycling (Open/Closed), providing the dynamic fluidity necessary for the assembly to remain within a functional 'viscoelastic window'. In this window, MORC2 achieves the local density required for DNA compaction and gene silencing*

Supplemental Figures

Fig. S1 Full-length MORC2 is a dimeric protein, with dimerization mediated by its C-terminal CC3 domain.

*(**a**) Negative-stain electron microscopy revealed that MORC2FL particles purified from HEK293F cells appeared poorly resolved and exhibited considerable morphological heterogeneity. And a zoomed-in particle was to comparing morphology from negative stain EM with AlphaFold predicted structure. Scaler bar: 100 nm and 10 nm.*

*(**b**) Structural prediction of MORC2FL using AlphaFold3 under a two-copy modeling condition revealed the presence of an extended disordered region at the C-terminus and suggested a potential dimerization interface within this region.*

*(**c**) Summary of theoretical and measured molecular weight of MORC2 constructs, including MORC2FL, MORC2ΔCC3-IBD, CC3-IBD, CC3, and CC3 mutants. Data are derived from recombinant protein purification and static light-scattering (SLS) analysis.*

*(**d**) AlphaFold3-based modeling of MORC2 with the N-terminal domain removed revealed structural features of the C-terminus, including extensive disorder and a putative dimerization interface.*

*(**e**) Molecular model of the CC3 dimer highlights hydrophobic core residues (I908, L911, L915, F921, F922, F951, Y954). Key intermolecular distances include I908-I908' (3.4 Å), L911-L915' (3.7 Å), F922-F922' (3.9 Å) and L958-L958' (4.0 Å), supporting dimer stability.*

*(**f**) Molecular model of the CC3 dimer formation interface show the additional hydrophobic interactions.*

*(**g**) Point mutations in key residues (L911, L915, F922) affect dimerization. Additional mutants (I908Q, F951Q, Y921A, Y954A, L958Q) show no significant change in molecular weight compared to WT, confirming their minimal impact on dimer formation. SLS analysis shows molecular weight distributions, with WT CC3-IBD forming dimers (~ 60 kDa) as indicated by red curves, while mutants exhibit higher molecular weights indicative of aggregation. Constructs were tagged with a Trx tag (14 kDa) for solubility.*

Fig. S2 In vitro and in vivo evidence that MORC2 undergoes phase separation.

*(**a**) Concentration gradients of EGFP-MORC2FL proteins (0.9, 1.8, 3.6, and 7.2 μM) were analyzed for in vitro phase separation. The proteins were examined in a buffer containing 150 mM NaCl, and phase separation was characterized by fluorescence microscopy with 488 nm excitation for EGFP. Scaler bar: 2 μm.*

*(**b**) SDS-PAGE analysis of EGFP-MORC2FL in sedimentation-based assays. Protein distribution between supernatant (S) and pellet (P) fractions is shown for increasing concentrations (0.9, 1.8, 3.6, and 7.2 μM).*

*(**c**) Time-lapse imaging of EGFP-MORC2FL phase separation over 120 s highlights dynamic droplet fusion. Scaler bar: 2 μm.*

*(**d**) Schematic of CRISPR-Cas9 strategy for generating MORC2 knockout (KO) HeLa cells. sgRNA targeting sequences and protospacer adjacent motifs (PAM) are highlighted. Genomic sequencing confirms insertion-deletion mutations introduced at target sites in MORC2 allelic genes.*

*(**e**) Immunostaining images of WT and MORC2 KO HeLa cells validate the specificity of the custom-made MORC2 antibody. Scaler bar: 5 μm.*

*(**f**) The fusion of condensates of EGFP-MORC2 over expression in HeLa cell.*

Fig. S3 Genomic loci of MORC2a in chimeric mice and its subcellular localization during mitosis.

(a) *Generation of endogenous EGFP-MORC2 chimeric mice. Genomic sequencing confirms insertion-EGFP mutations introduced at target sites in MORC2 allelic genes.*

(b) *Live-cell imaging revealed that EGFP-MORC2FL exhibits dynamic subcellular localization throughout mitosis, without forming detectable condensates. Scaler bar: 10 μm.*

Fig. S4 The C-terminal domain (CTD) of MORC2 mediates nuclear condensate formation.

(a) *EGFP-tagged MORC2 CTD forms nuclear condensates in HeLa cells, whereas the NTD does not. Scaler bar: 10 μm.*

(b) *Truncation analysis of EGFP-tagged CTD reveals that both the CC3-IBD and IDR-NLS regions are important for condensate formation. Scaler bar: 10 μm.*

(c) *EGFP-tagged CTD constructs lacking the IDR-NLS region but fused to an exogenous N-terminal nuclear localization signal ("PKKKRKV") successfully localize to the nucleus but fail to form condensates, indicating that the IDR is essential for phase separation. Scaler bar: 10 μm.*

(d) *Targeted expression of IDR-NLS and CC3-IBD fragments in the nucleus failed to induce condensate formation, indicating that these domains alone are not sufficient to drive phase separation. Scaler bar: 10 μm.*

(e) *The statistical data for droplet area in (Fig. 3a) demonstrate that the deletion of IDR or CC3 is imperative for condensate formation. The data are expressed as the mean ± standard error of the mean (SEM). n ≥ 15 fields; one-way ANOVA with Tukey's post hoc test. ****P < 0.0001.*

Fig. S5 The biophysical behavior of CTD and CTDΔCW in vitro.

(a) *SDS-PAGE analysis of Cy3-labeled CTD showing expected size and degradative behavior.*

(b) *Fluorescence microscopy images of Cy3-labeledCTD at increasing protein concentrations (1.25□μM, 2.5□μM, 5□μM, and 10□μM) in standard phase separation buffer (50□mM Tris-Cl, pH 8.0, 150□mM NaCl). Despite increasing concentration, CW-CTD formed only small, dense puncta that did not exhibit robust size expansion or morphological changes. Scaler bar: 10 μm.*

(c) *Representative bright-field and Cy3 fluorescence microscopy images of labeled CTDΔCW protein droplets, showing intact condensate morphology under standard phase separation conditions. Scaler bar: 5 μm.*

(d) *SDS-PAGE analysis comparing Cy3-labeled and unlabeled CTDΔCW, indicating no degradation or mobility shift.*

(e) *Static light scattering (SLS) profiles of Cy3-labeled and unlabeled CTDΔCW proteins reveal similar molecular weight distributions and hydrodynamic behavior.*

(f) *Time-lapse imaging of Cy3-labeled CTDΔCW over 180 s reveals dynamic droplet behavior in vitro. Scaler bar: 2 μm.*

Fig. S6 In vitro assays to investigate isolated fragment fails to induce phase separation.

(a) *Sedimentation assay showing domain containing 1-900 (5μM) and 1-900 (5μM) is not induced phase separation in 100 mM NaCl buffer.*

(b) *Representative images showing that Cy3-labeled MORC2 1-900 (5μM) could not undergo phase separation.*

*(**c**) In vitro assays to investigate the contribution of IDR-IBD interactions to phase separation.*
*(**d**) Sedimentation assay showing domain containing 1-536 (10 μM) and 537-1032 (10 μM) is not induced phase separation in 100 mM NaCl buffer.*
*(**e**) Representative images showing that Cy3-labeled MORC2 1-536 (10μM) could not undergo phase separation in including 50 nM 601 DNA.*

Fig. S7 NMR titration about IDR-IBD. *The corresponding CSP plots in the process of NMR titration related to Fig. 4*

Fig. S8 Phase diagram of MORC2-DNA.
DNA-dependent phase behavior of the protein in vitro. Phase diagram showing the formation of liquid droplets and amorphous structures as a function of DNA and protein concentrations. Each circle represents an individual experimental condition. Black regions indicate regimes favoring liquid droplet formation, whereas the darker shaded region at high DNA and protein concentrations denotes the formation of amorphous assemblies. At low protein concentration (0.5 μM) and low DNA levels, no phase separation was observed in shaded regions.

Fig. S9 IBD-deficient mutant (ΔIBD) in HEK293T cells
(a) Representative single-cell images of EGFP-MORC2-expressing HEK293T cells. Scaler bar: 10 μm.
*(b) Quantification of the percentage of cells showing visible nuclear condensates in each construct. Data are presented as mean ± SEM; n ≥ 11 replicates. Statistical significance was assessed using unpaired Student's t-test. ****p < 0.0001.*

Fig. S10 Condensation and dynamics-defective MORC2 mutants impair transcriptional regulation
(a) *GO-based molecular function terms enriched among all differentially expressed genes upon EGFP-MORC2FL overexpression.*
(b) *Venn diagram illustrating the overlap between differentially expressed genes identified in this study and previously characterized targets regulated in MORC2 knockout HeLa cells[12]. Fold-change (log fold change) analysis of the 102 overlapping genes showing significant expression changes upon MORC2FL overexpression, compared with their corresponding fold changes following overexpression of the three MORC2 mutants. Dashed lines connect the same gene across the four transfection conditions.*

Fig. S11 Compared to the wild-type protein, N-terminally truncated MORC2-CTD forms nuclear puncta in HeLa cells with significantly reduced internal dynamics, as revealed by FRAP assays.

Fig. S12 Representative SDS-PAGE gels for all purified protein constructs.
*(**a**) MORC2 fragments used for conformational analysis by FPLC-MALS (related to Fig. 1).*
*(**b**) MORC2 CC3 domain fragments used for dimerization analysis by FPLC-MALS (related to Fig. S1).*
*(**c**) MORC2 fragments expressed in E. coli for EMSA-based DNA-binding assays (related to Fig. 5).*
*(**d**) MORC2 fragments expressed in HEK293F cells for ATPase activity measurements with or without 601 DNA (related to Fig. 5).*

*(**e**) Disease-associated MORC2 mutants expressed in HEK293F cells for ATPase and DNA-binding assays, while E236G mutant exhibited poor biochemical properties, precluding further analysis in vitro (related to Fig. 7).*

*(**f**) Agarose gel analysis for MORC2 constructs to confirm the absence of nucleic acids. The pET32 vector as the positive control, the protein preparation for analysis is 0.05 mg.*

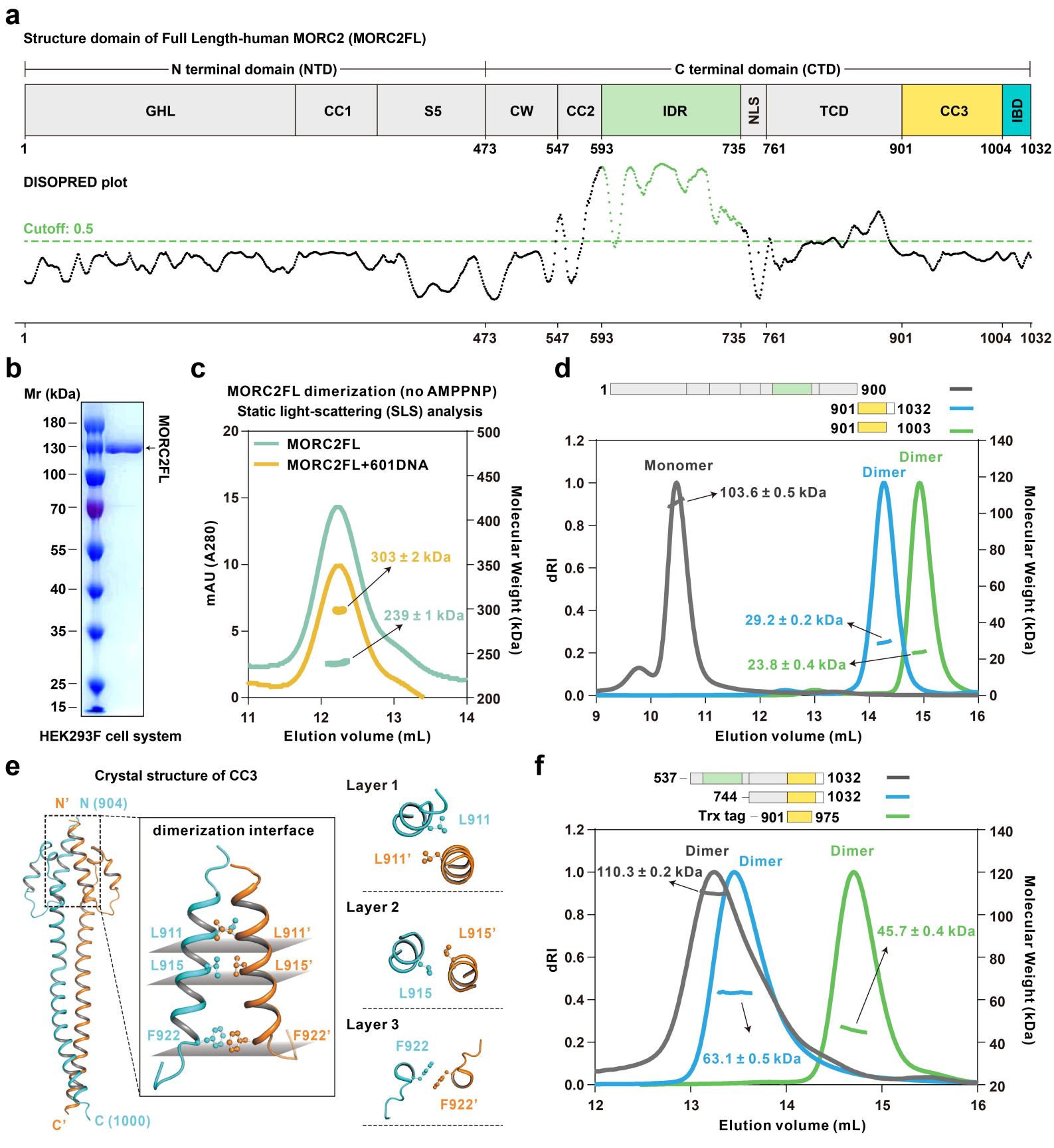
a
Structure domain of Full Length-human MORC2 (MORC2FL)
N terminal domain (NTD)
C terminal domain (CTD)
GHL
CC1
S5
CW
CC2
IDR
NLS
TCD
CC3
IBD
1
473
547
593
735
761
901
1004
1032
DISOPRED plot
Cutoff: 0.5
b
Mr (kDa)
180
130
100
70
55
40
35
25
15
MORC2FL
HEK293F cell system
c
MORC2FL dimerization (no AMPPNP)
Static light-scattering (SLS) analysis
MORC2FL
MORC2FL+601DNA
303 ± 2 kDa
239 ± 1 kDa
mAU (A280)
Molecular Weight (kDa)
Elution volume (mL)
d
1
900
901
1032
901
1003
Monomer
Dimer
Dimer
103.6 ± 0.5 kDa
29.2 ± 0.2 kDa
23.8 ± 0.4 kDa
dRI
Molecular Weight (kDa)
Elution volume (mL)
e
Crystal structure of CC3
N' N (904)
C' C (1000)
dimerization interface
L911
L911'
L915
L915'
F922
F922'
Layer 1
L911
L911'
Layer 2
L915'
L915
Layer 3
F922
F922'
f
537
1032
744
1032
Trx tag
901
975
Dimer
Dimer
Dimer
110.3 ± 0.2 kDa
45.7 ± 0.4 kDa
63.1 ± 0.5 kDa
dRI
Molecular Weight (kDa)
Elution volume (mL)

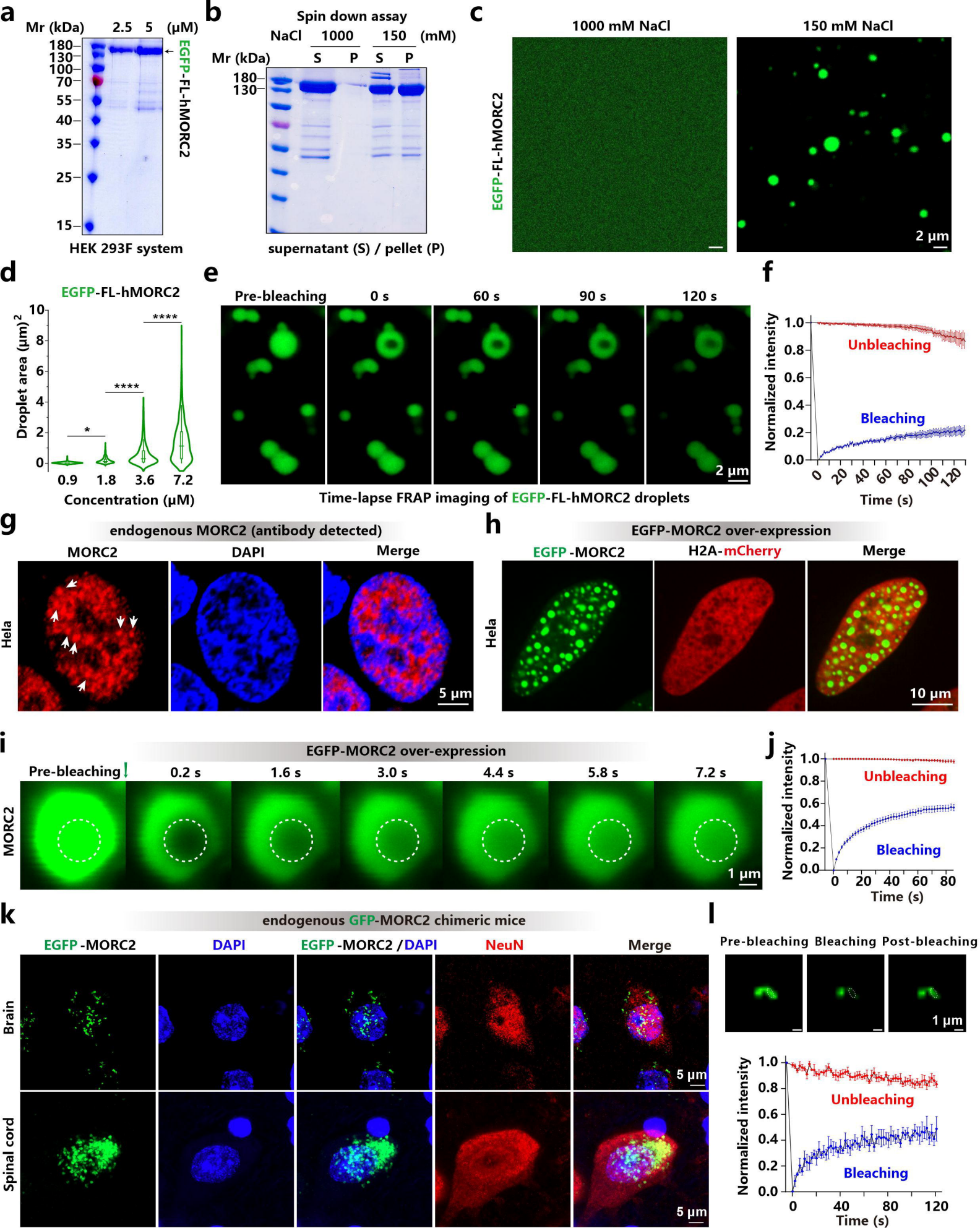
a
Mr (kDa)
2.5
5
(μM)
180
130
100
70
55
40
35
25
15
EGFP-FL-hMORC2
HEK 293F system
b
Spin down assay
NaCl
1000
150
(mM)
Mr (kDa)
S
P
S
P
180
130
supernatant (S) / pellet (P)
c
1000 mM NaCl
150 mM NaCl
EGFP-FL-hMORC2
2 μm
d
EGFP-FL-hMORC2
Droplet area (μm)²
10
8
6
4
2
0
*
****
****
0.9
1.8
3.6
7.2
Concentration (μM)
e
Pre-bleaching
0 s
60 s
90 s
120 s
2 μm
Time-lapse FRAP imaging of EGFP-FL-hMORC2 droplets
f
Normalized intensity
1.0
0.8
0.6
0.4
0.2
0.0
Unbleaching
Bleaching
0
20
40
60
80
100
120
Time (s)
g
endogenous MORC2 (antibody detected)
MORC2
DAPI
Merge
Hela
5 μm
h
EGFP-MORC2 over-expression
EGFP -MORC2
H2A-mCherry
Merge
Hela
10 μm
i
EGFP-MORC2 over-expression
Pre-bleaching
0.2 s
1.6 s
3.0 s
4.4 s
5.8 s
7.2 s
MORC2
1 μm
j
Normalized intensity
1.0
0.8
0.6
0.4
0.2
0.0
Unbleaching
Bleaching
0
20
40
60
80
Time (s)
k
endogenous GFP-MORC2 chimeric mice
EGFP -MORC2
DAPI
EGFP -MORC2 / DAPI
NeuN
Merge
Brain
Spinal cord
5 μm
5 μm
l
Pre-bleaching
Bleaching
Post-bleaching
1 μm
Normalized intensity
1.0
0.8
0.6
0.4
0.2
0.0
Unbleaching
Bleaching
0
40
80
120
Time (s)

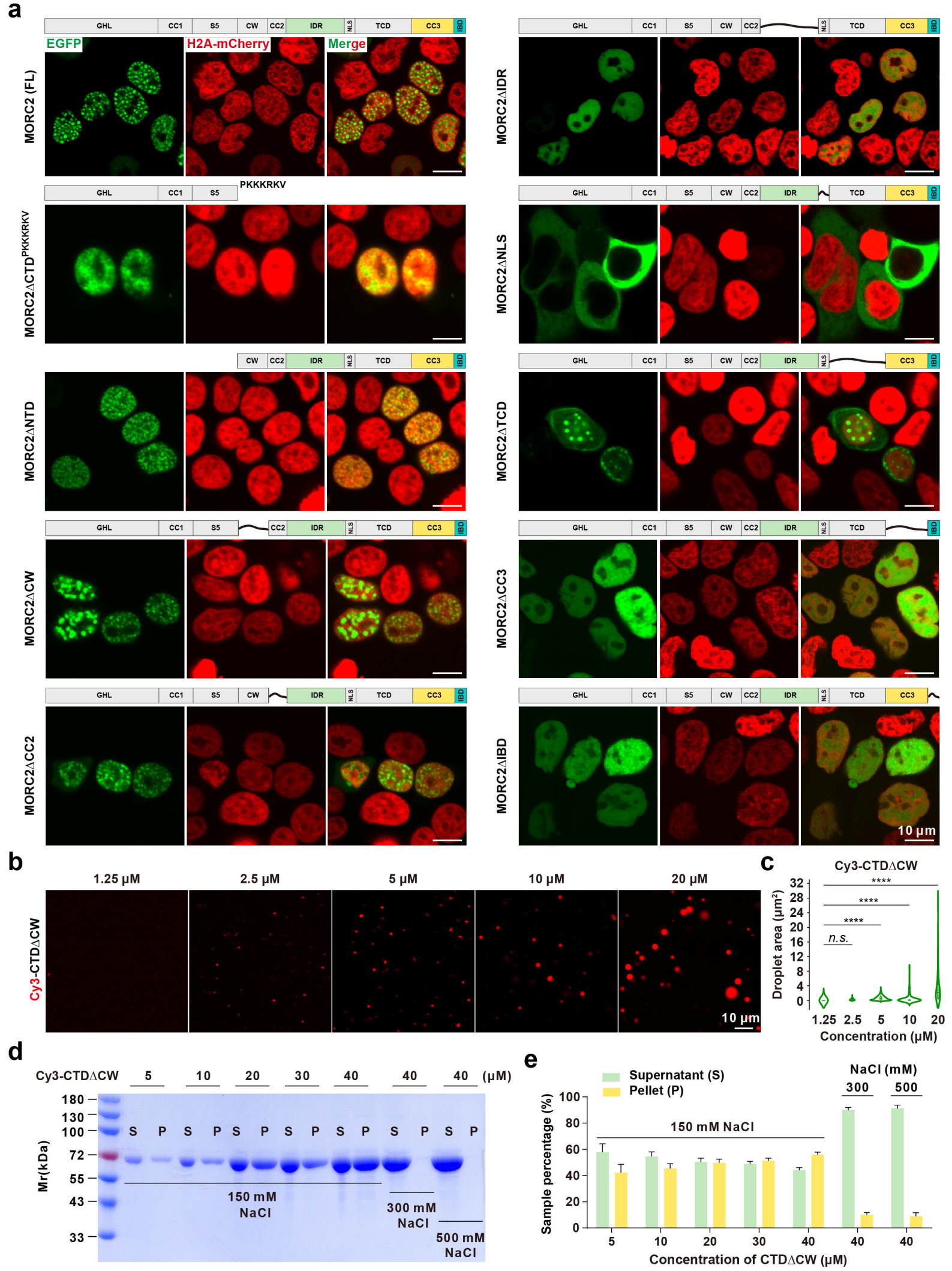
a
GHL
CC1
S5
CW
CC2
IDR
NLS
TCD
CC3
IBD
EGFP
H2A-mCherry
Merge
MORC2 (FL)
MORC2ΔIDR
PKKKRKV
MORC2ΔCTD^PKKKRKV
MORC2ΔNLS
MORC2ΔNTD
MORC2ΔTCD
MORC2ΔCW
MORC2ΔCC3
MORC2ΔCC2
MORC2ΔIBD
10 μm
b
1.25 μM
2.5 μM
5 μM
10 μM
20 μM
Cy3-CTDΔCW
10 μm
c
Cy3-CTDΔCW
Droplet area (μm²)
****
n.s.
1.25
2.5
5
10
20
Concentration (μM)
d
Cy3-CTDΔCW
5
10
20
30
40
40
40
(μM)
180
130
100
72
55
43
33
Mr(kDa)
S
P
150 mM NaCl
300 mM NaCl
500 mM NaCl
e
Supernatant (S)
Pellet (P)
NaCl (mM)
300
500
150 mM NaCl
Sample percentage (%)
Concentration of CTDΔCW (μM)

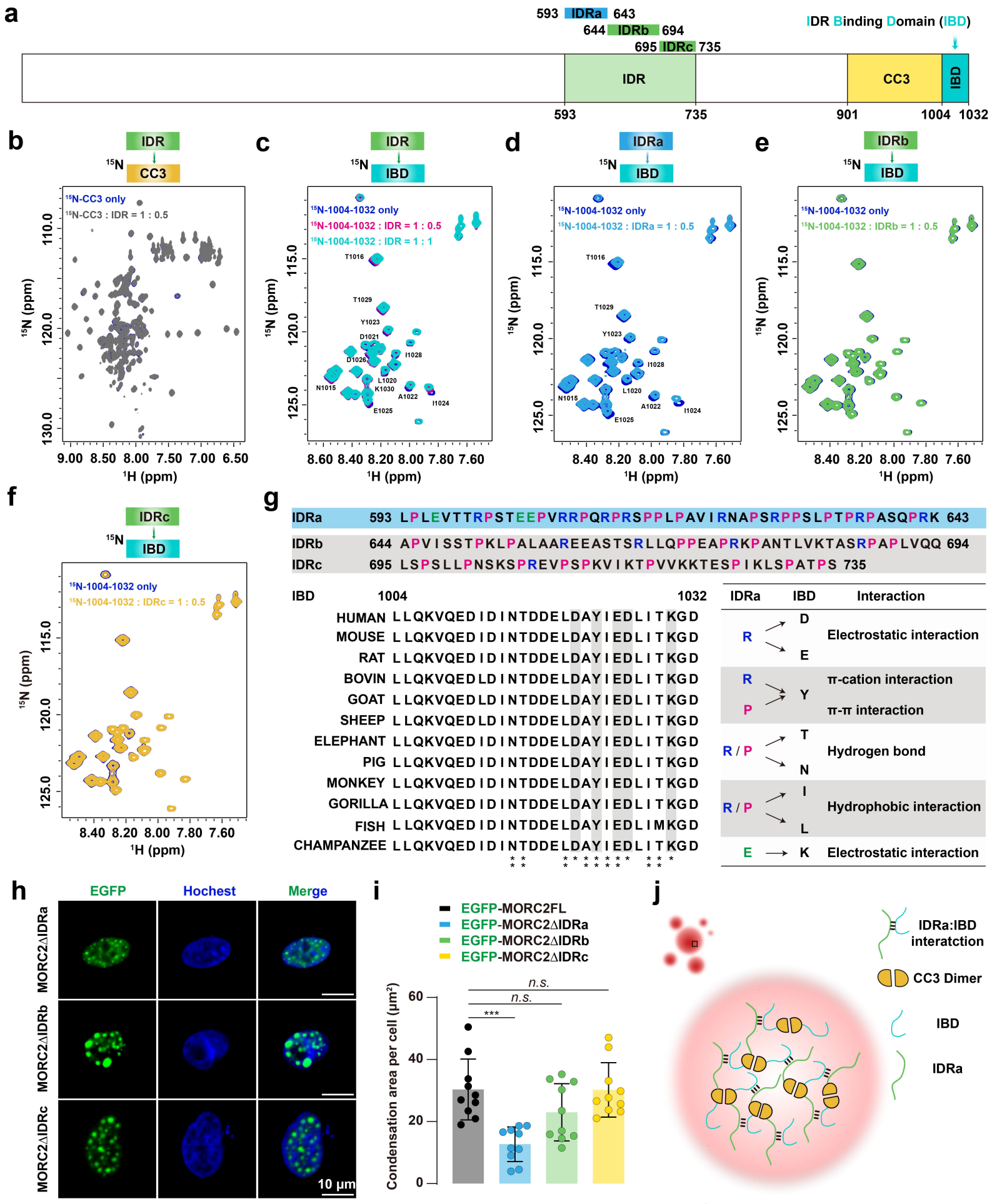
a
593 IDRa 643
644 IDRb 694
695 IDRc 735
IDR Binding Domain (IBD)
IDR
CC3
IBD
593
735
901
1004
1032
b
IDR
15N
CC3
15N-CC3 only
15N-CC3 : IDR = 1 : 0.5
15N (ppm)
1H (ppm)
c
IDR
15N
IBD
15N-1004-1032 only
15N-1004-1032 : IDR = 1 : 0.5
15N-1004-1032 : IDR = 1 : 1
T1016
T1029
Y1023
D1021
D1026
I1028
L1020
K1030
N1015
A1022
I1024
E1025
d
IDRa
15N
IBD
15N-1004-1032 only
15N-1004-1032 : IDRa = 1 : 0.5
e
IDRb
15N
IBD
15N-1004-1032 only
15N-1004-1032 : IDRb = 1 : 0.5
f
IDRc
15N
IBD
15N-1004-1032 only
15N-1004-1032 : IDRc = 1 : 0.5
g
IDRa 593 LPLEVTTRPSTEEPVRRPQRPRSPPLPAVIRNAPSRPPSLPTPRPASQPRK 643
IDRb 644 APVISSTPKLPALAAREEASTSRLLQPPEAPRKPANTLVKTASRPAPLVQQ 694
IDRc 695 LSPSLLPNSKSPREVPSPKVIKTPVVKKTESPIKLSPATPS 735
IBD 1004 1032
HUMAN LLQKVQEDIDINTDDELDAYIEDLITKGD
MOUSE LLQKVQEDIDINTDDELDAYIEDLITKGD
RAT LLQKVQEDIDINTDDELDAYIEDLITKGD
BOVIN LLQKVQEDLDINTDDELDAYIEDLITKGD
GOAT LLQKVQEDLDINTDDELDAYIEDLITKGD
SHEEP LLQKVQEDLDINTDDELDAYIEDLITKGD
ELEPHANT LLQKVQEDIDINTDDELDAYIEDLITKGD
PIG LLQKVQEDIDINTDDELDAYIEDLITKGD
MONKEY LLQKVQEDIDINTDDELDAYIEDLITKGD
GORILLA LLQKVQEDIDINTDDELDAYIEDLITKGD
FISH LLQKVQEDIDINTDDELDAYIEDLIMKGD
CHAMPANZEE LLQKVQEDIDINTDDELDAYIEDLITKGD
IDRa IBD Interaction
R D Electrostatic interaction
R E
R Y π-cation interaction
P Y π-π interaction
R / P T Hydrogen bond
R / P N
R / P I Hydrophobic interaction
R / P L
E K Electrostatic interaction
h
EGFP
Hochest
Merge
MORC2ΔIDRa
MORC2ΔIDRb
MORC2ΔIDRc
10 μm
i
EGFP-MORC2FL
EGFP-MORC2ΔIDRa
EGFP-MORC2ΔIDRb
EGFP-MORC2ΔIDRc
n.s.
n.s.
***
Condensation area per cell (μm²)
60
40
20
0
j
IDRa:IBD interatction
CC3 Dimer
IBD
IDRa

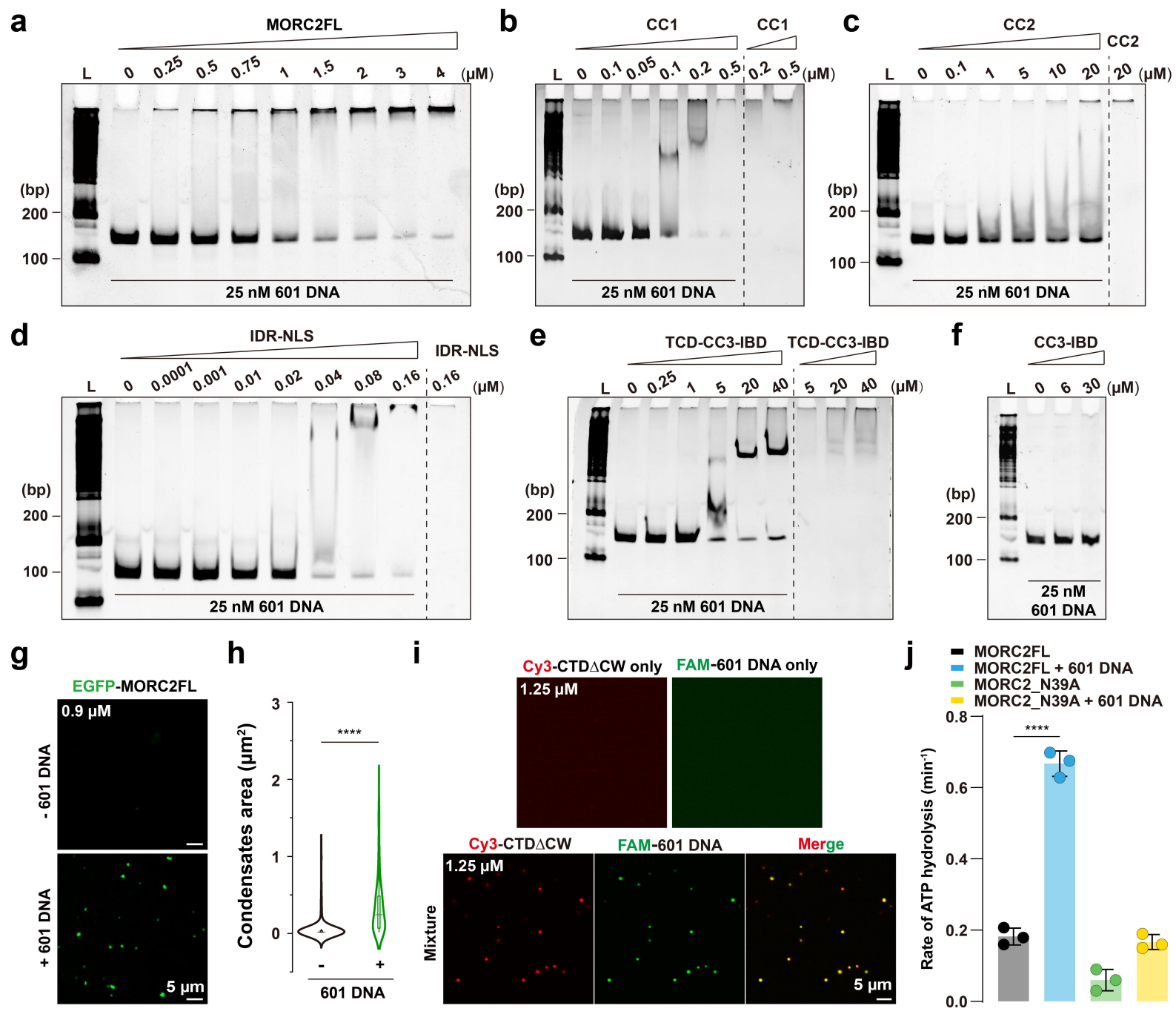
a
MORC2FL
L 0 0.25 0.5 0.75 1 1.5 2 3 4 (μM)
(bp)
200
100
25 nM 601 DNA
b
CC1
CC1
L 0 0.1 0.05 0.1 0.2 0.5 0.2 0.5 (μM)
(bp)
200
100
25 nM 601 DNA
c
CC2
CC2
L 0 0.1 1 5 10 20 20 (μM)
(bp)
200
100
25 nM 601 DNA
d
IDR-NLS
IDR-NLS
L 0 0.0001 0.001 0.01 0.02 0.04 0.08 0.16 0.16 (μM)
(bp)
200
100
25 nM 601 DNA
e
TCD-CC3-IBD
TCD-CC3-IBD
L 0 0.25 1 5 20 40 5 20 40 (μM)
(bp)
200
100
25 nM 601 DNA
f
CC3-IBD
L 0 6 30 (μM)
(bp)
200
100
25 nM
601 DNA
g
EGFP-MORC2FL
0.9 μM
- 601 DNA
+ 601 DNA
5 μm
h
Condensates area (μm²)
3
2
1
0
****
-
+
601 DNA
i
Cy3-CTDΔCW only
FAM-601 DNA only
1.25 μM
Cy3-CTDΔCW
FAM-601 DNA
Merge
Mixture
1.25 μM
5 μm
j
MORC2FL
MORC2FL + 601 DNA
MORC2_N39A
MORC2_N39A + 601 DNA
Rate of ATP hydrolysis (min⁻¹)
0.8
0.6
0.4
0.2
0.0
****

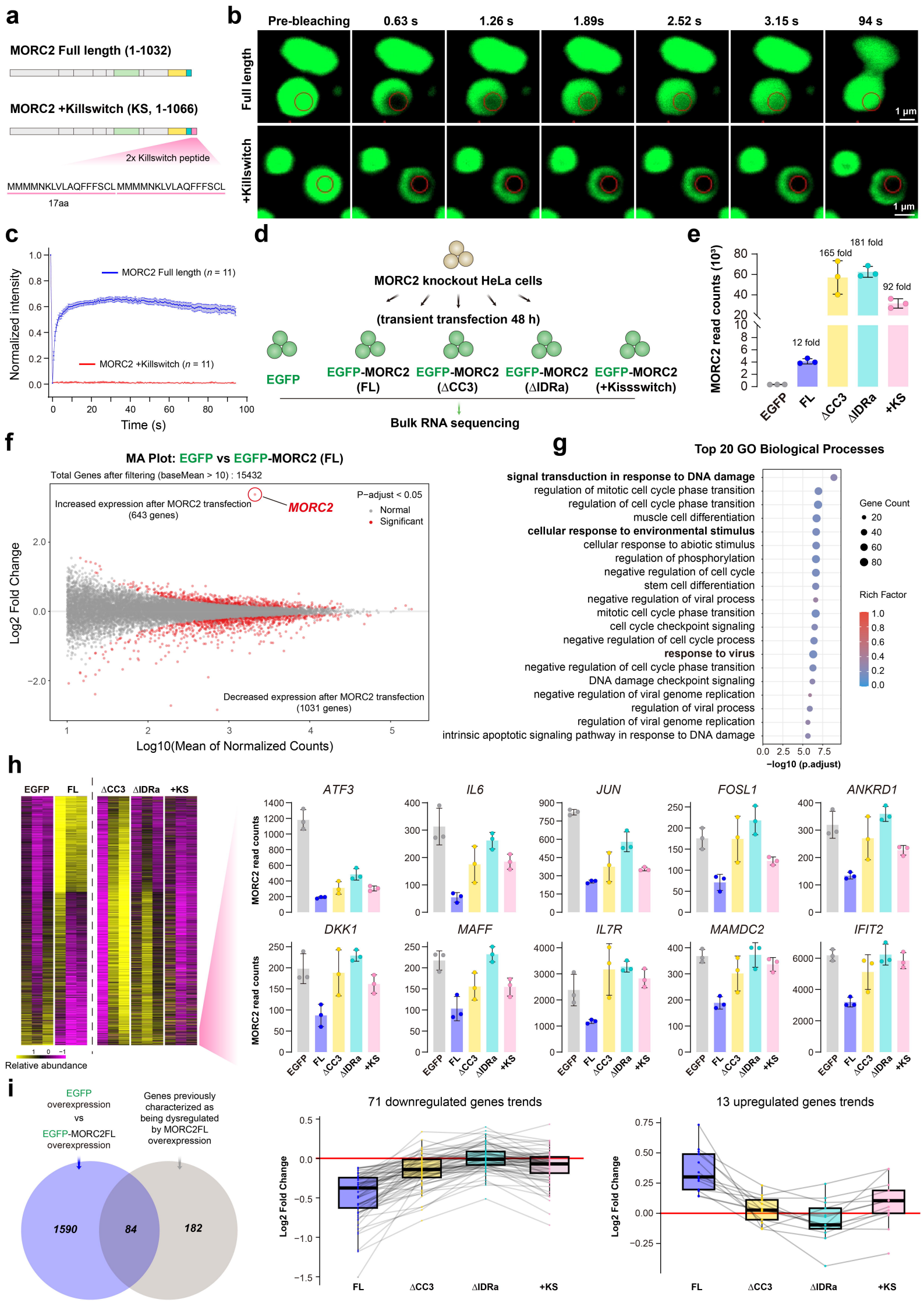
a
MORC2 Full length (1-1032)
MORC2 +Killswitch (KS, 1-1066)
2x Killswitch peptide
MMMMNKLVLAQFFFSCL MMMMNKLVLAQFFFSCL
17aa
b
Pre-bleaching
0.63 s
1.26 s
1.89s
2.52 s
3.15 s
94 s
Full length
+Killswitch
1 μm
c
Normalized intensity
MORC2 Full length (n = 11)
MORC2 +Killswitch (n = 11)
Time (s)
d
MORC2 knockout HeLa cells
(transient transfection 48 h)
EGFP
EGFP-MORC2 (FL)
EGFP-MORC2 (ΔCC3)
EGFP-MORC2 (ΔIDRa)
EGFP-MORC2 (+Kissswitch)
Bulk RNA sequencing
e
MORC2 read counts (10³)
181 fold
165 fold
92 fold
12 fold
EGFP
FL
ΔCC3
ΔIDRa
+KS
f
MA Plot: EGFP vs EGFP-MORC2 (FL)
Total Genes after filtering (baseMean > 10) : 15432
Increased expression after MORC2 transfection (643 genes)
MORC2
P−adjust < 0.05
Normal
Significant
Decreased expression after MORC2 transfection (1031 genes)
Log2 Fold Change
Log10(Mean of Normalized Counts)
g
Top 20 GO Biological Processes
signal transduction in response to DNA damage
regulation of mitotic cell cycle phase transition
regulation of cell cycle phase transition
muscle cell differentiation
cellular response to environmental stimulus
cellular response to abiotic stimulus
regulation of phosphorylation
negative regulation of cell cycle
stem cell differentiation
negative regulation of viral process
mitotic cell cycle phase transition
cell cycle checkpoint signaling
negative regulation of cell cycle process
response to virus
negative regulation of cell cycle phase transition
DNA damage checkpoint signaling
negative regulation of viral genome replication
regulation of viral process
regulation of viral genome replication
intrinsic apoptotic signaling pathway in response to DNA damage
−log10 (p.adjust)
Gene Count
Rich Factor
h
EGFP
FL
ΔCC3
ΔIDRa
+KS
Relative abundance
ATF3
IL6
JUN
FOSL1
ANKRD1
DKK1
MAFF
IL7R
MAMDC2
IFIT2
MORC2 read counts
i
EGFP overexpression vs EGFP-MORC2FL overexpression
Genes previously characterized as being dysregulated by MORC2FL overexpression
1590
84
182
71 downregulated genes trends
13 upregulated genes trends
Log2 Fold Change

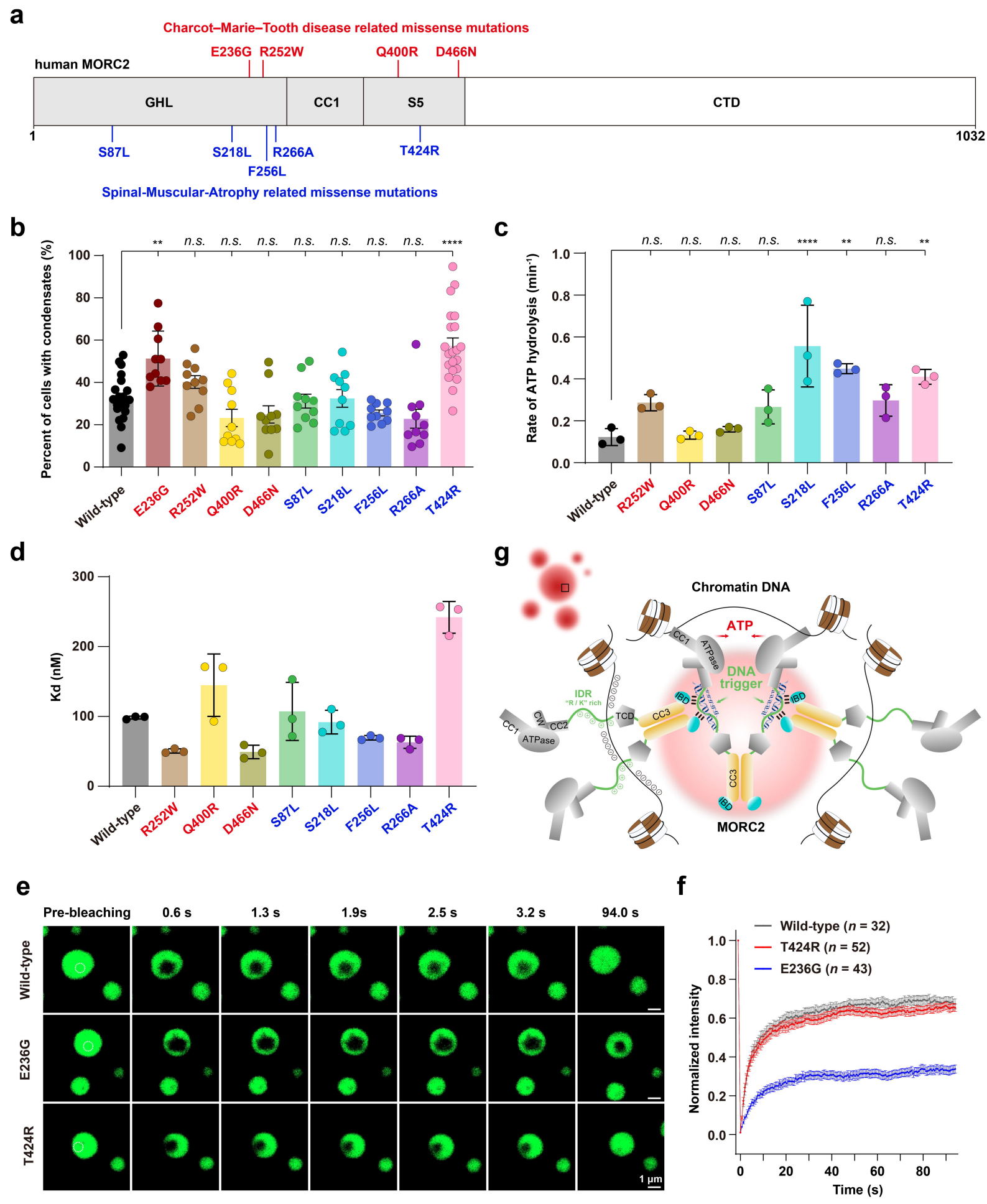
a
Charcot–Marie–Tooth disease related missense mutations
E236G
R252W
Q400R
D466N
human MORC2
GHL
CC1
S5
CTD
1
1032
S87L
S218L
R266A
F256L
T424R
Spinal-Muscular-Atrophy related missense mutations
b
Percent of cells with condensates (%)
Wild-type
E236G
R252W
Q400R
D466N
S87L
S218L
F256L
R266A
T424R
c
Rate of ATP hydrolysis (min⁻¹)
d
Kd (nM)
g
Chromatin DNA
ATP
DNA trigger
IDR
"R / K" rich
CC1
ATPase
CW
CC2
TCD
CC3
IBD
MORC2
e
Pre-bleaching
0.6 s
1.3 s
1.9s
2.5 s
3.2 s
94.0 s
Wild-type
E236G
T424R
1 μm
f
Wild-type (n = 32)
T424R (n = 52)
E236G (n = 43)
Normalized intensity
Time (s)

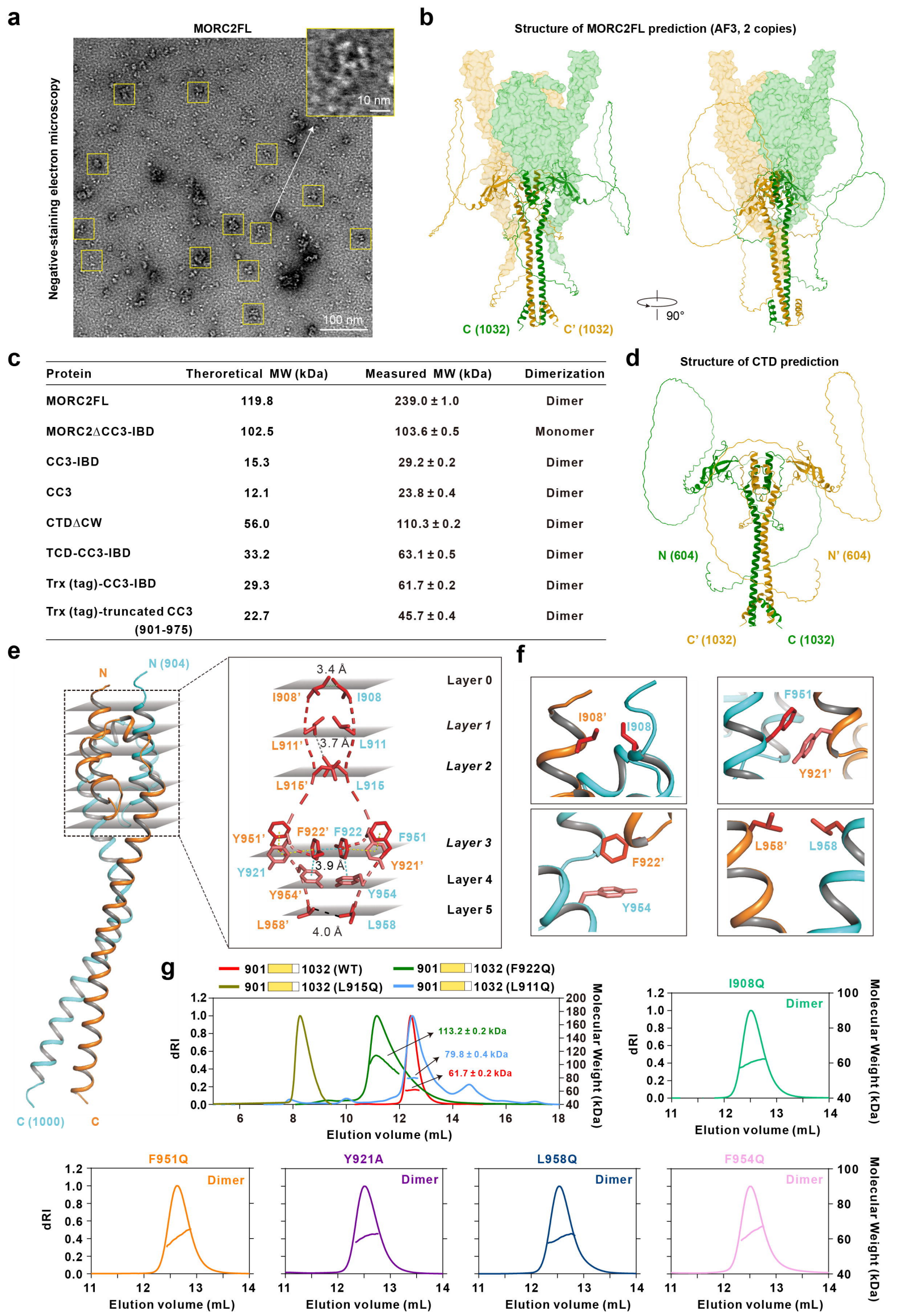

Protein	Theroretical MW (kDa)	Measured MW (kDa)	Dimerization
MORC2FL	119.8	239.0 ± 1.0	Dimer
MORC2ΔCC3-IBD	102.5	103.6 ± 0.5	Monomer
CC3-IBD	15.3	29.2 ± 0.2	Dimer
CC3	12.1	23.8 ± 0.4	Dimer
CTDΔCW	56.0	110.3 ± 0.2	Dimer
TCD-CC3-IBD	33.2	63.1 ± 0.5	Dimer
Trx (tag)-CC3-IBD	29.3	61.7 ± 0.2	Dimer
Trx (tag)-truncated CC3 (901-975)	22.7	45.7 ± 0.4	Dimer

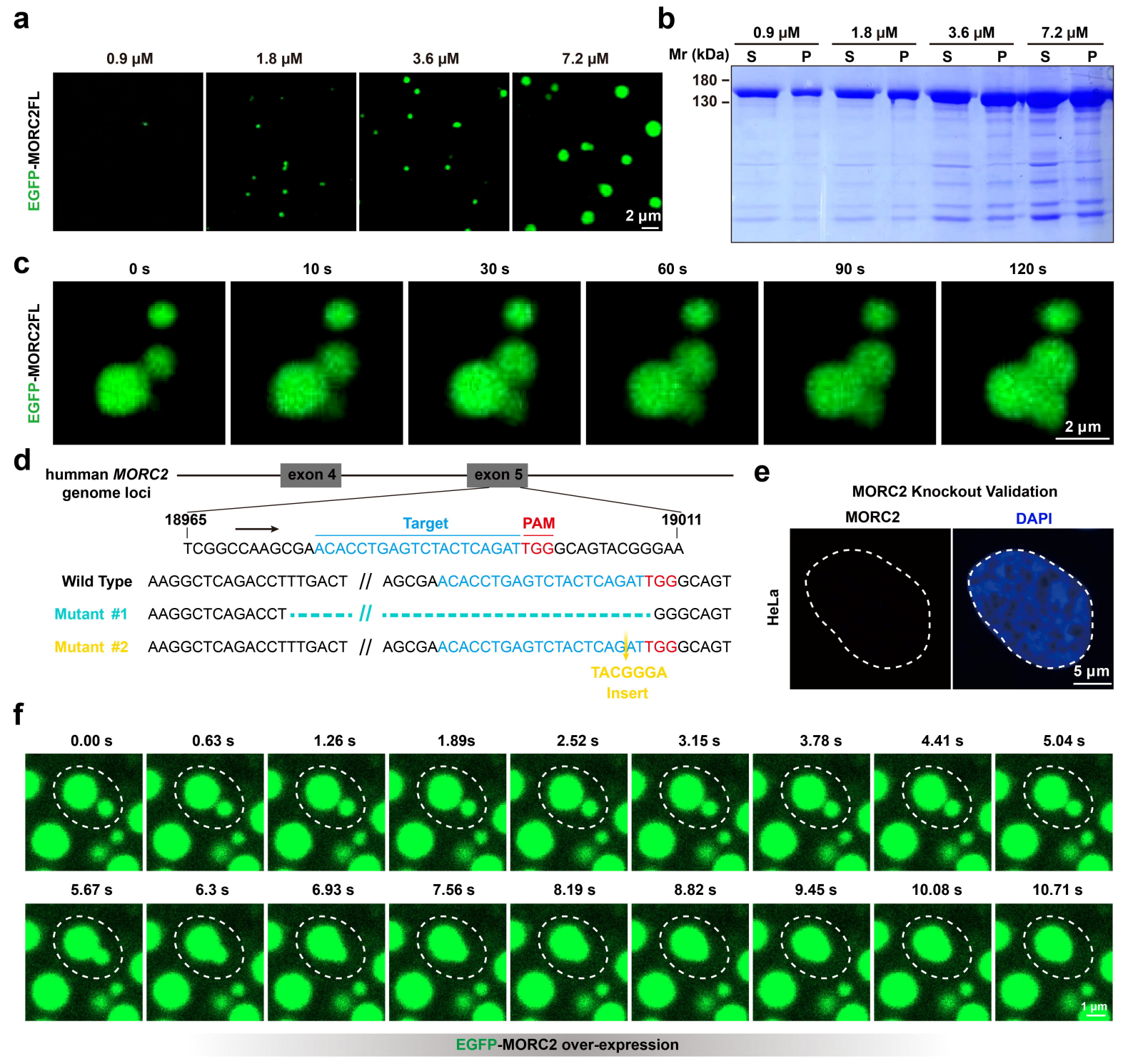
a
0.9 μM
1.8 μM
3.6 μM
7.2 μM
EGFP-MORC2FL
2 μm
b
0.9 μM
1.8 μM
3.6 μM
7.2 μM
Mr (kDa)
S
P
180
130
c
0 s
10 s
30 s
60 s
90 s
120 s
EGFP-MORC2FL
2 μm
d
humman MORC2 genome loci
exon 4
exon 5
18965
19011
Target
PAM
TCGGCCAAGCGAACACCTGAGTCTACTCAGATTGGGCAGTACGGGAA
Wild Type AAGGCTCAGACCTTTGACT // AGCGAACACCTGAGTCTACTCAGATTGGGCAGT
Mutant #1 AAGGCTCAGACCT // GGGCAGT
Mutant #2 AAGGCTCAGACCTTTGACT // AGCGAACACCTGAGTCTACTCAGATTGGGCAGT
TACGGGA
Insert
e
MORC2 Knockout Validation
MORC2
DAPI
HeLa
5 μm
f
0.00 s
0.63 s
1.26 s
1.89s
2.52 s
3.15 s
3.78 s
4.41 s
5.04 s
5.67 s
6.3 s
6.93 s
7.56 s
8.19 s
8.82 s
9.45 s
10.08 s
10.71 s
1 μm
EGFP-MORC2 over-expression

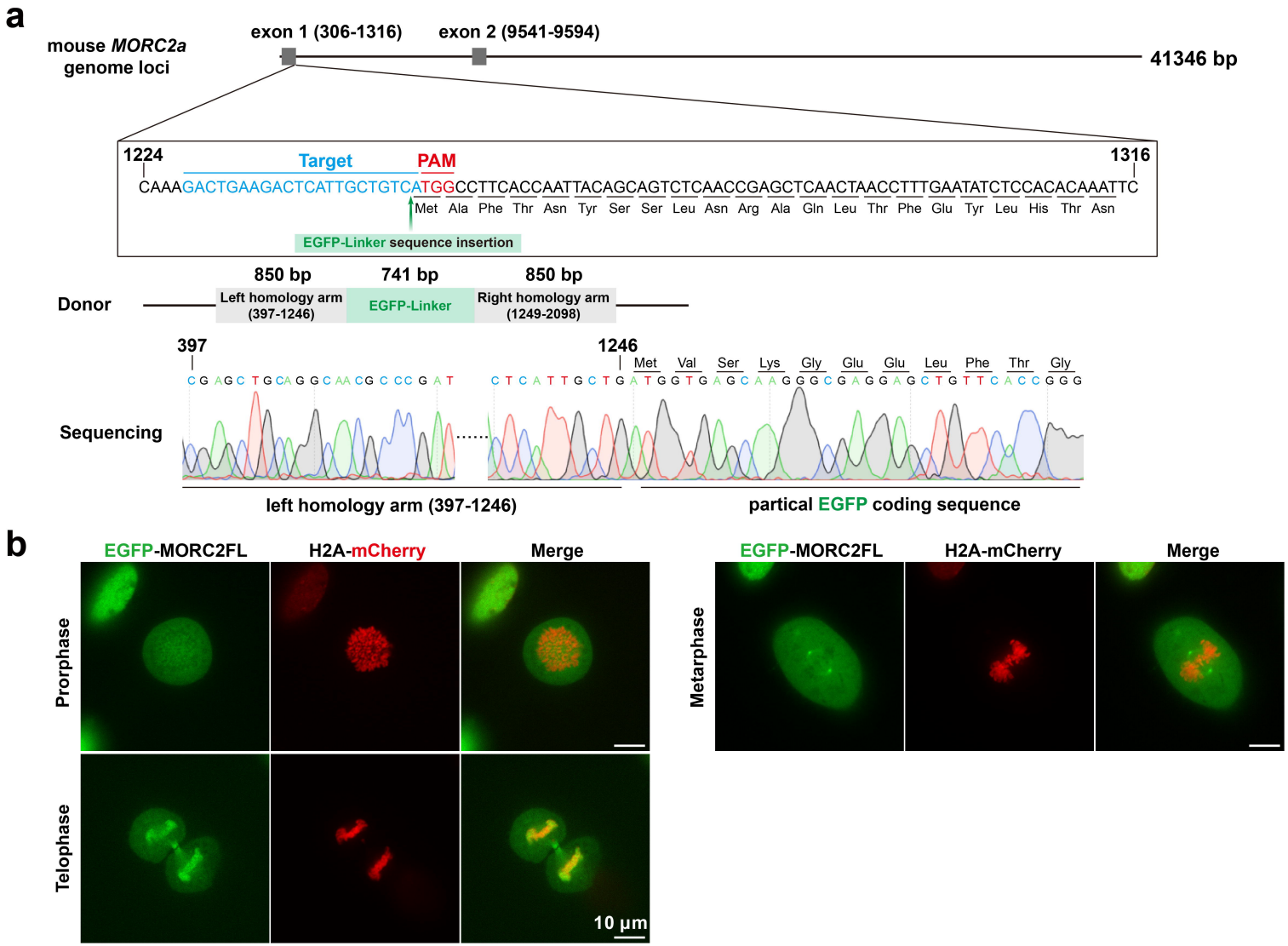
a
mouse MORC2a genome loci
exon 1 (306-1316)
exon 2 (9541-9594)
41346 bp
1224
Target
PAM
1316
CAAAGACTGAAGACTCATTGCTGTCATGGCCTTCACCAATTACAGCAGTCTCAACCGAGCTCAACTAACCTTTGAATATCTCCACACAAATTC
Met Ala Phe Thr Asn Tyr Ser Ser Leu Asn Arg Ala Gln Leu Thr Phe Glu Tyr Leu His Thr Asn
EGFP-Linker sequence insertion
Donor
850 bp
741 bp
850 bp
Left homology arm (397-1246)
EGFP-Linker
Right homology arm (1249-2098)
397
1246
Met Val Ser Lys Gly Glu Glu Leu Phe Thr Gly
Sequencing
left homology arm (397-1246)
partical EGFP coding sequence
b
EGFP-MORC2FL
H2A-mCherry
Merge
Prorphase
Telophase
10 μm
EGFP-MORC2FL
H2A-mCherry
Merge
Metarphase

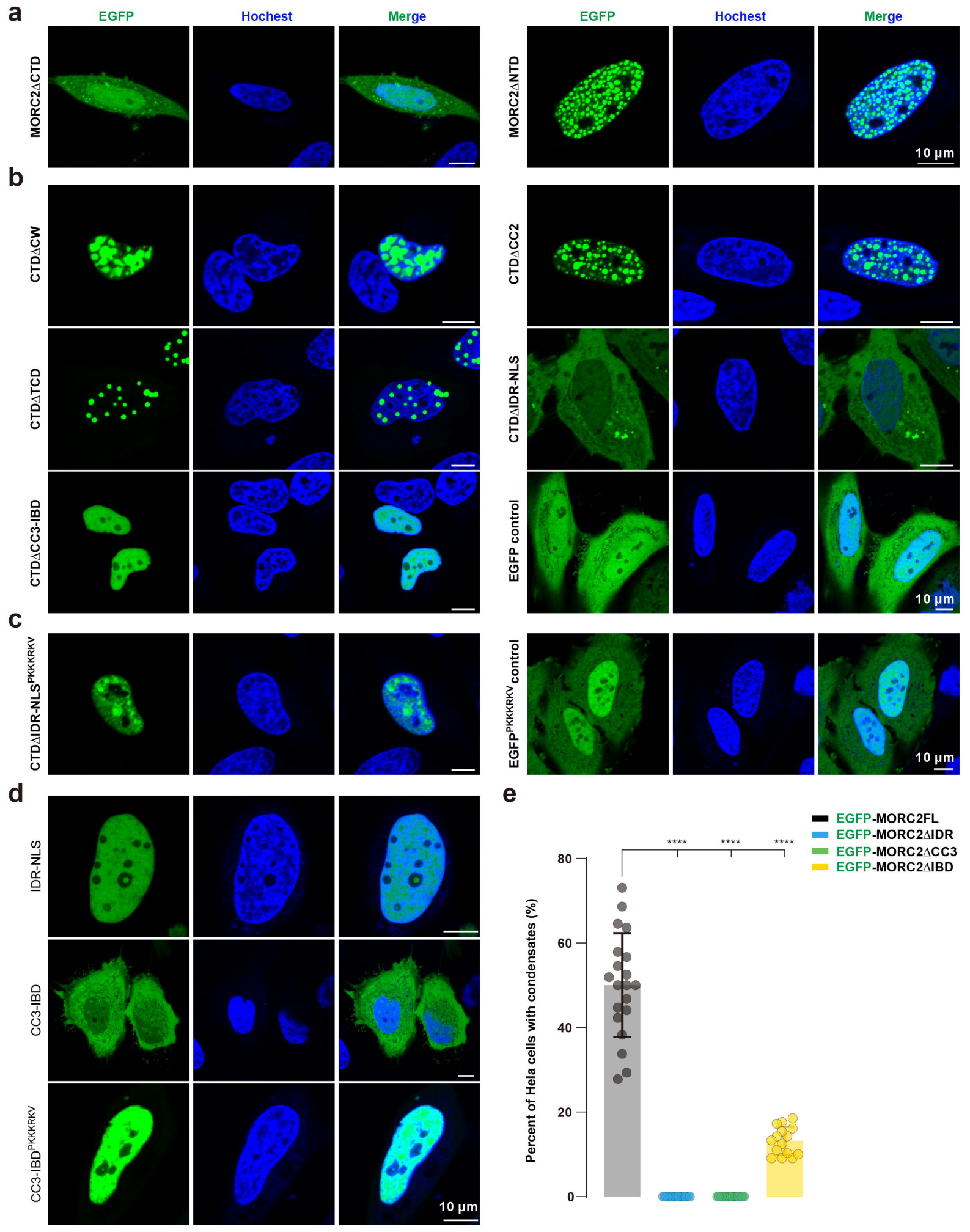
a
EGFP
Hochest
Merge
MORC2ΔCTD
MORC2ΔNTD
10 μm
b
CTDΔCW
CTDΔCC2
CTDΔTCD
CTDΔIDR-NLS
CTDΔCC3-IBD
EGFP control
10 μm
c
CTDΔIDR-NLSPKKKRKV
EGFPPKKKRKV control
10 μm
d
IDR-NLS
CC3-IBD
CC3-IBDPKKKRKV
10 μm
e
EGFP-MORC2FL
EGFP-MORC2ΔIDR
EGFP-MORC2ΔCC3
EGFP-MORC2ΔIBD
****
****
****
Percent of Hela cells with condensates (%)
80
60
40
20
0

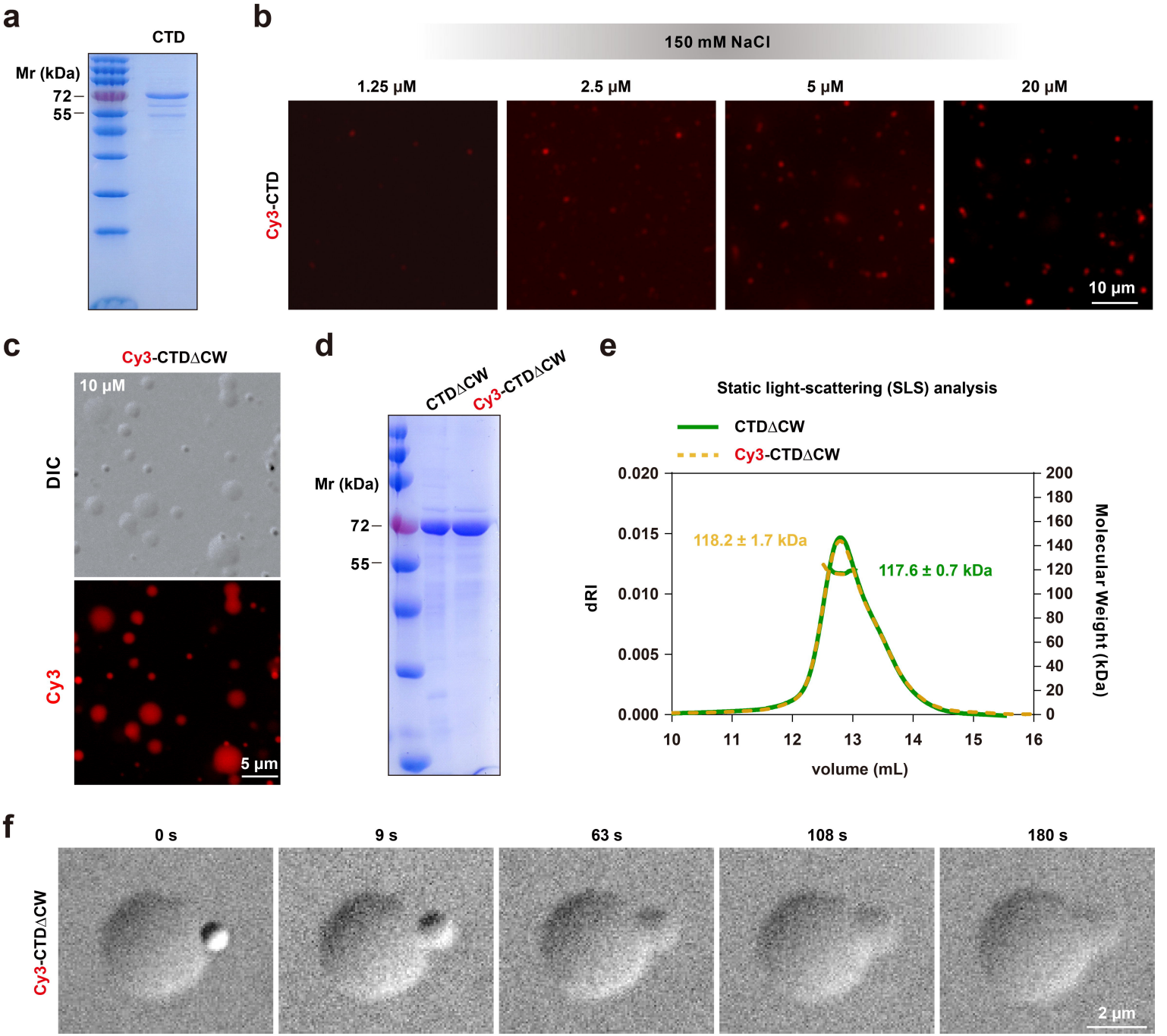
a
CTD
Mr (kDa)
72
55
b
150 mM NaCl
1.25 μM
2.5 μM
5 μM
20 μM
Cy3-CTD
10 μm
c
Cy3-CTDΔCW
10 μM
DIC
Cy3
5 μm
d
CTDΔCW
Cy3-CTDΔCW
Mr (kDa)
72
55
e
Static light-scattering (SLS) analysis
CTDΔCW
Cy3-CTDΔCW
118.2 ± 1.7 kDa
117.6 ± 0.7 kDa
dRI
Molecular Weight (kDa)
volume (mL)
f
0 s
9 s
63 s
108 s
180 s
Cy3-CTDΔCW
2 μm

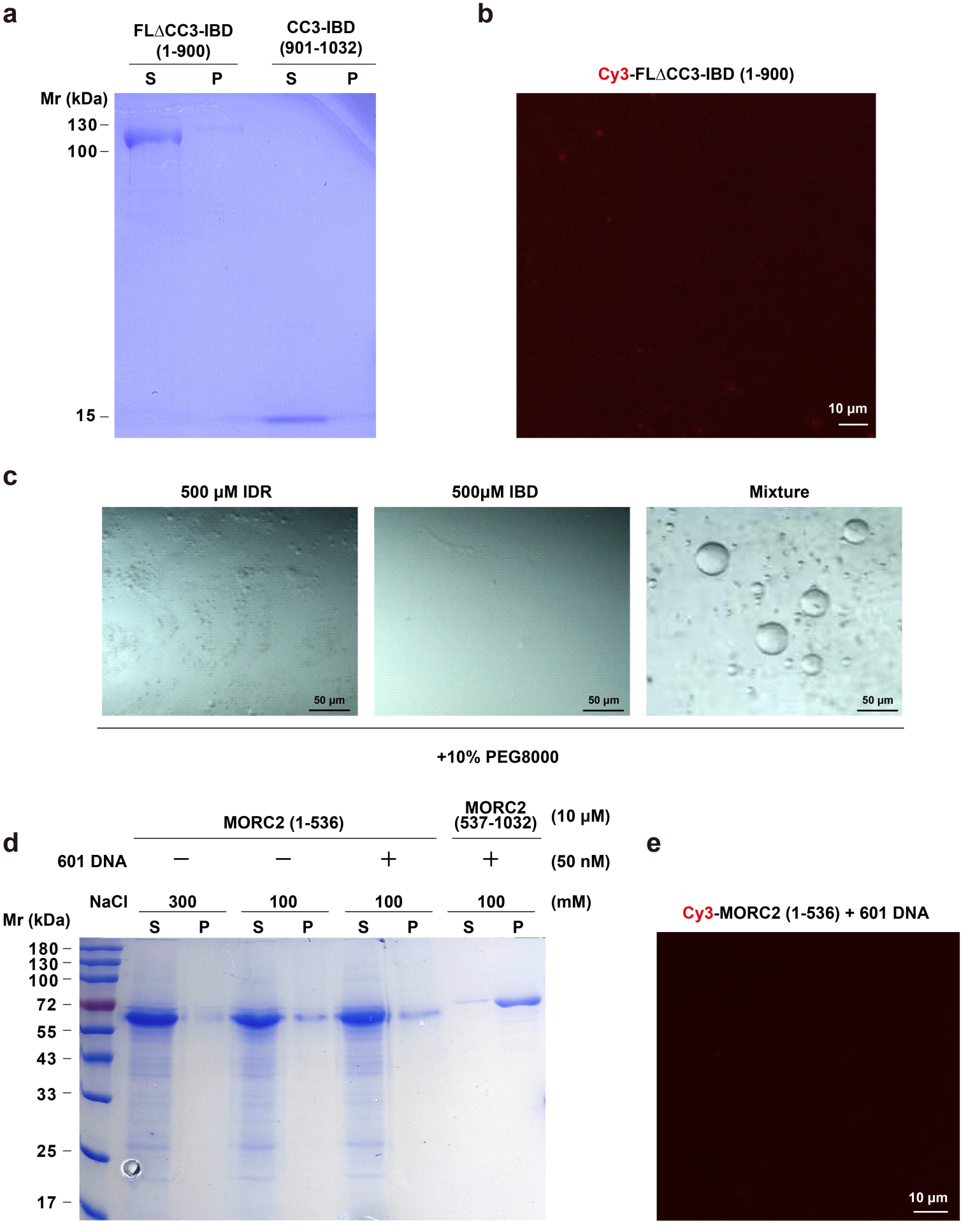
a
FLΔCC3-IBD (1-900)
CC3-IBD (901-1032)
S
P
S
P
Mr (kDa)
130
100
15
b
Cy3-FLΔCC3-IBD (1-900)
10 μm
c
500 μM IDR
500μM IBD
Mixture
50 μm
50 μm
50 μm
+10% PEG8000
d
MORC2 (1-536)
MORC2 (537-1032)
(10 μM)
601 DNA
−
−
+
+
(50 nM)
NaCl
300
100
100
100
(mM)
Mr (kDa)
S
P
S
P
S
P
S
P
180
130
100
72
55
43
33
25
17
e
Cy3-MORC2 (1-536) + 601 DNA
10 μm

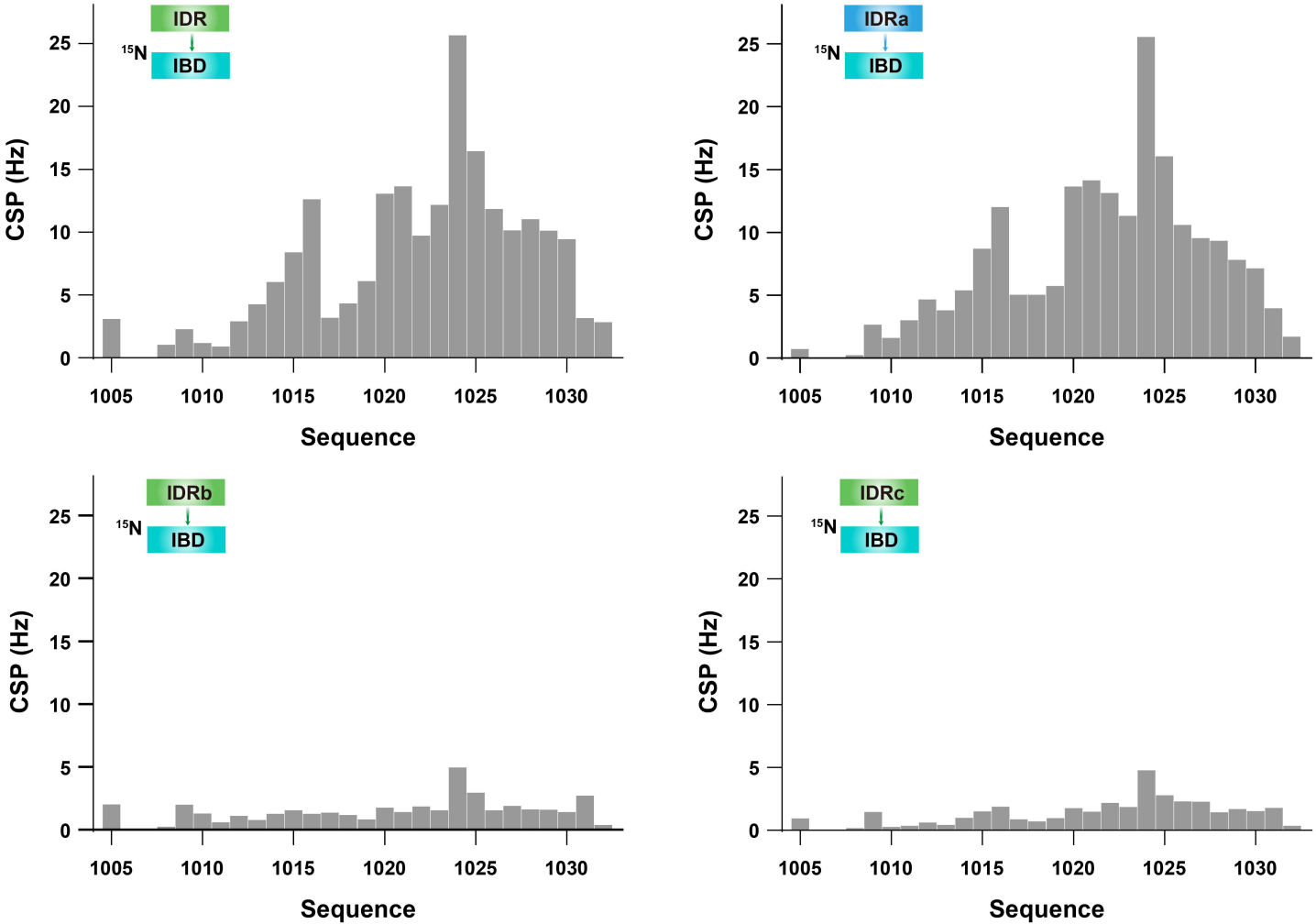
IDR
15N
IBD
CSP (Hz)
Sequence
IDRa
15N
IBD
CSP (Hz)
Sequence
IDRb
15N
IBD
CSP (Hz)
Sequence
IDRc
15N
IBD
CSP (Hz)
Sequence

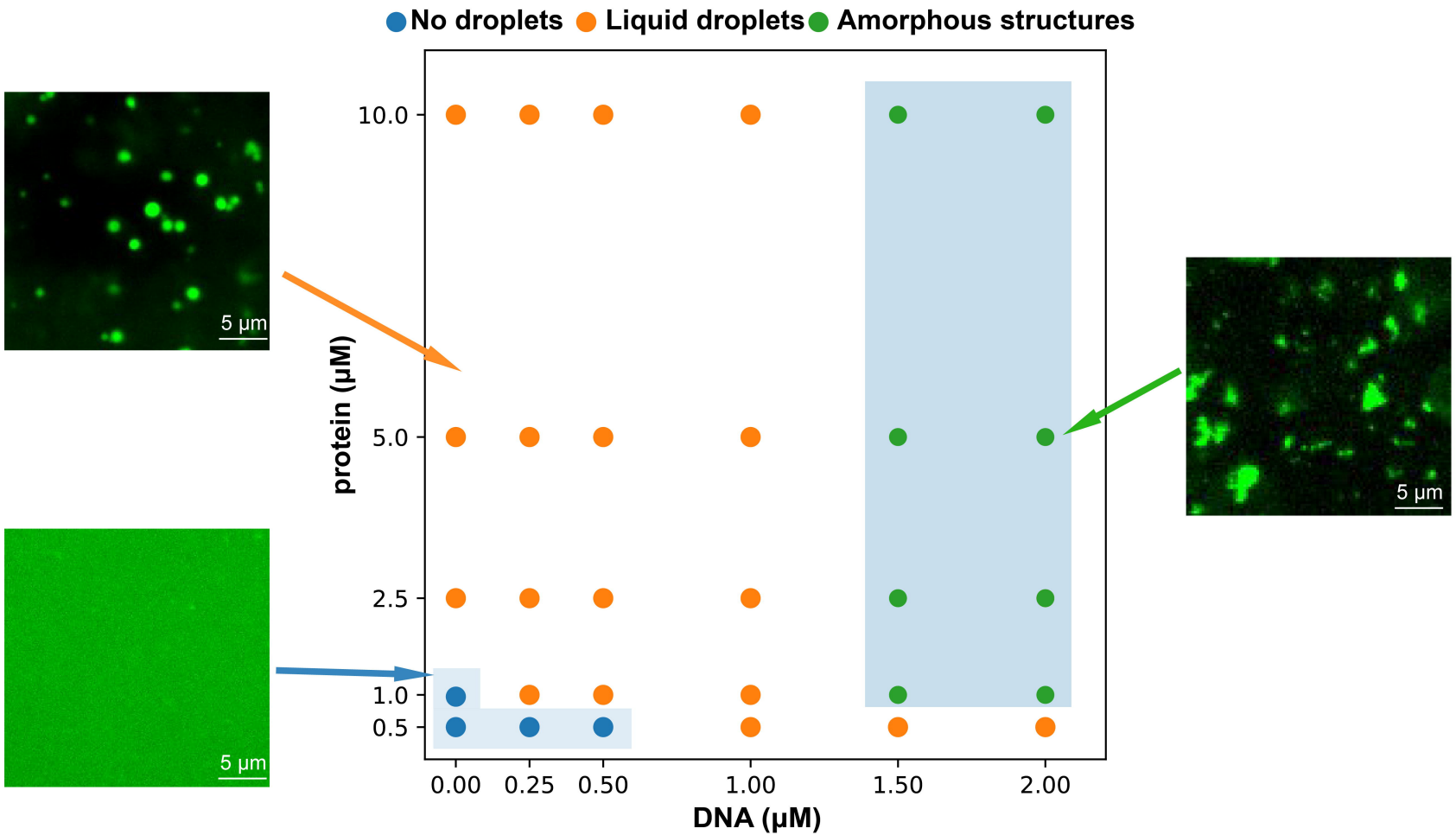
No droplets
Liquid droplets
Amorphous structures
protein (μM)
10.0
5.0
2.5
1.0
0.5
0.00
0.25
0.50
1.00
1.50
2.00
DNA (μM)
5 μm
5 μm
5 μm

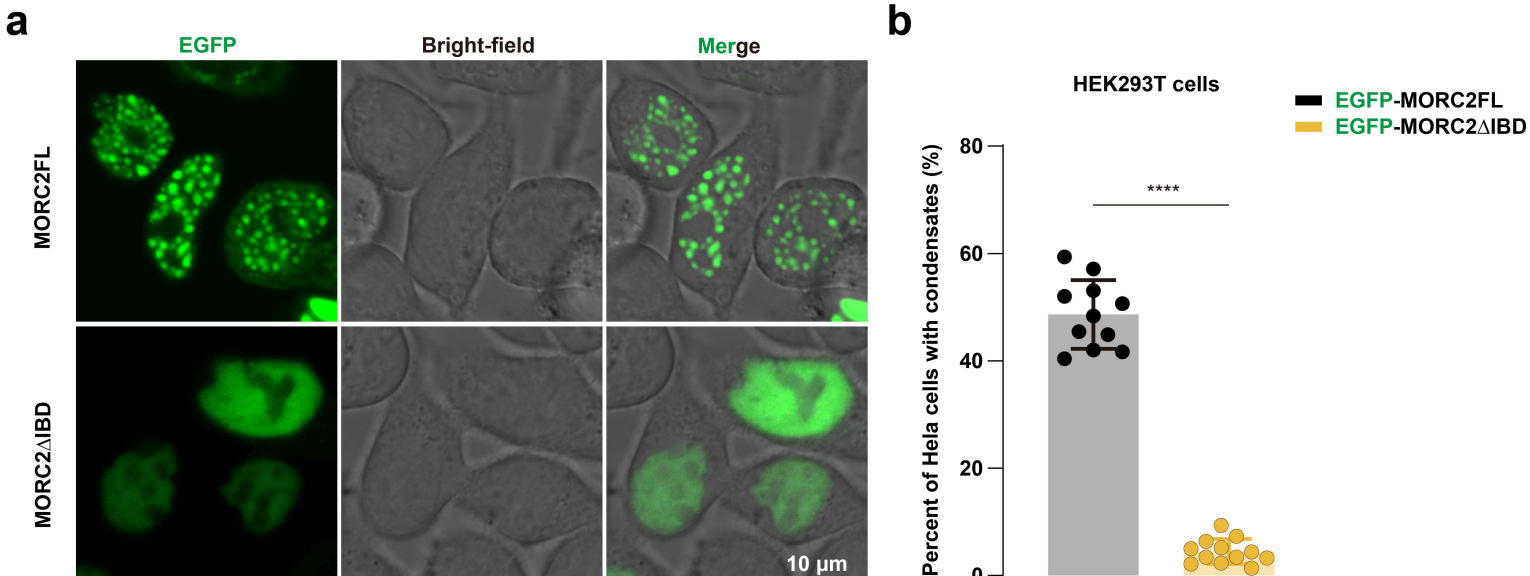
a
EGFP
Bright-field
Merge
MORC2FL
MORC2ΔIBD
10 µm
b
HEK293T cells
EGFP-MORC2FL
EGFP-MORC2ΔIBD
Percent of Hela cells with condensates (%)
80
60
40
20
0
****

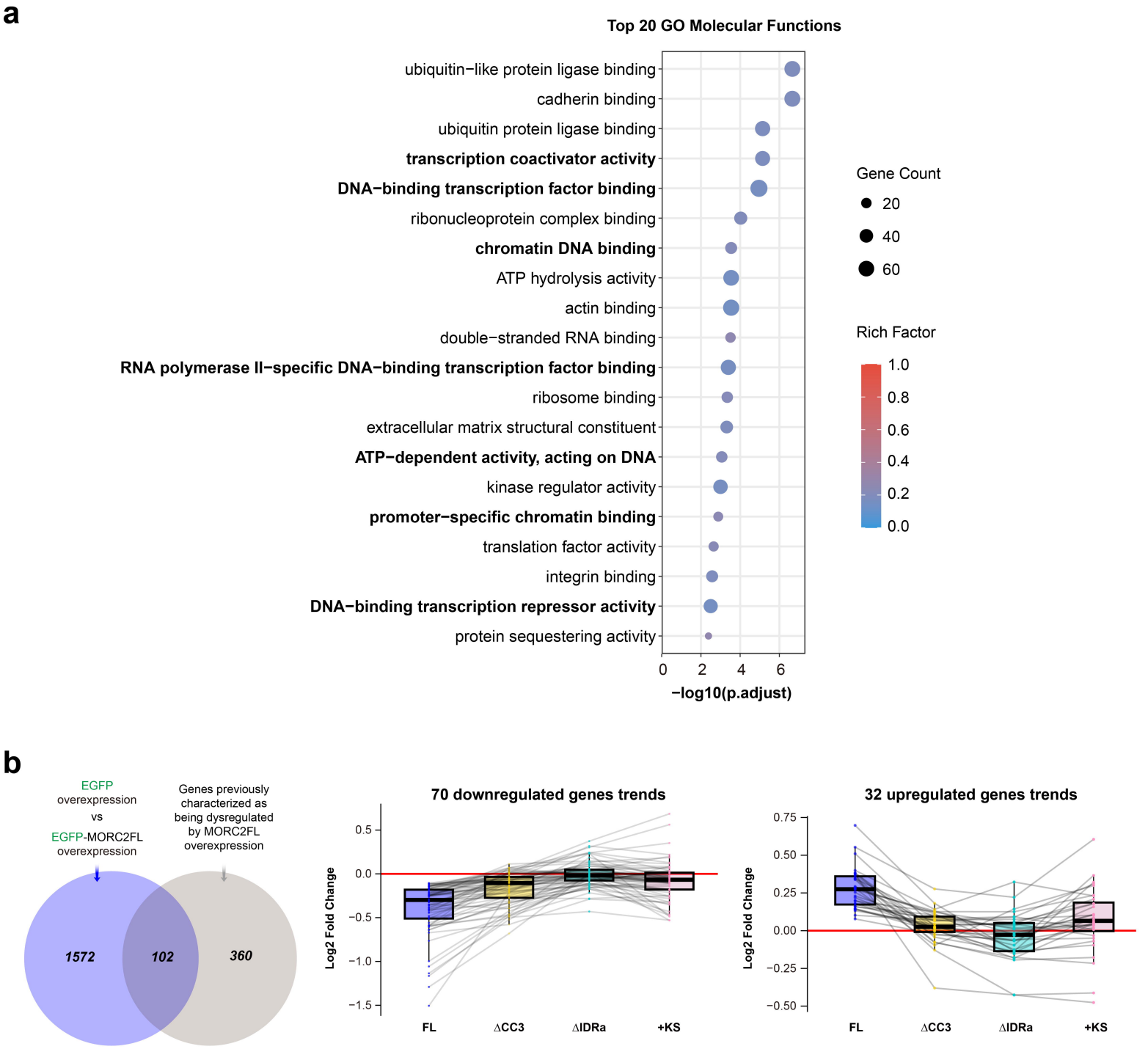
a
Top 20 GO Molecular Functions
ubiquitin−like protein ligase binding
cadherin binding
ubiquitin protein ligase binding
transcription coactivator activity
DNA−binding transcription factor binding
ribonucleoprotein complex binding
chromatin DNA binding
ATP hydrolysis activity
actin binding
double−stranded RNA binding
RNA polymerase II−specific DNA−binding transcription factor binding
ribosome binding
extracellular matrix structural constituent
ATP−dependent activity, acting on DNA
kinase regulator activity
promoter−specific chromatin binding
translation factor activity
integrin binding
DNA−binding transcription repressor activity
protein sequestering activity
0
2
4
6
−log10(p.adjust)
Gene Count
20
40
60
Rich Factor
1.0
0.8
0.6
0.4
0.2
0.0
b
EGFP overexpression vs EGFP-MORC2FL overexpression
Genes previously characterized as being dysregulated by MORC2FL overexpression
1572
102
360
70 downregulated genes trends
Log2 Fold Change
0.5
0.0
−0.5
−1.0
−1.5
FL
ΔCC3
ΔIDRa
+KS
32 upregulated genes trends
Log2 Fold Change
0.75
0.50
0.25
0.00
−0.25
−0.50
FL
ΔCC3
ΔIDRa
+KS

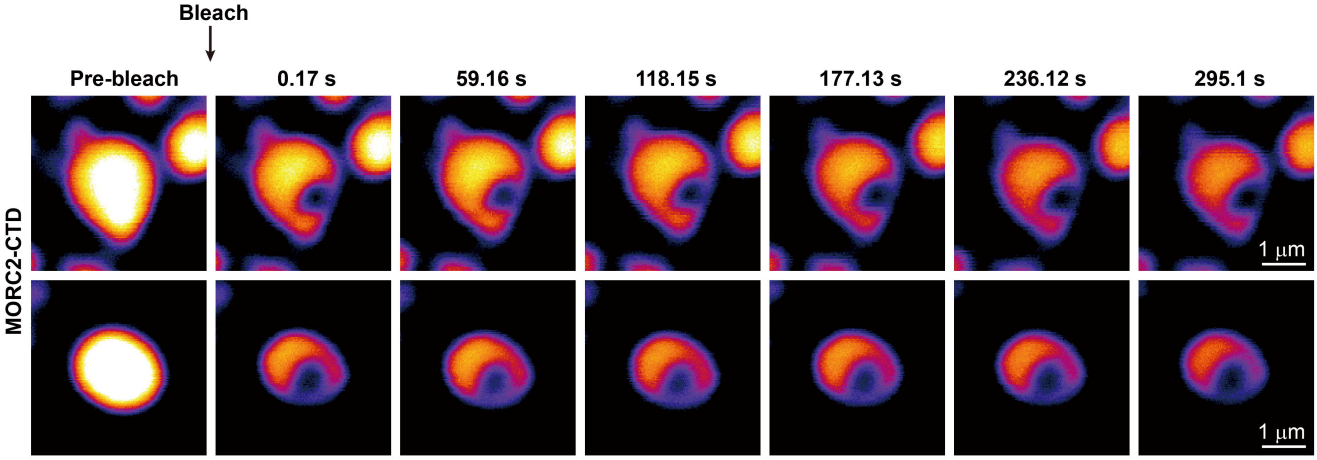
Bleach
Pre-bleach
0.17 s
59.16 s
118.15 s
177.13 s
236.12 s
295.1 s
MORC2-CTD
1 μm
1 μm

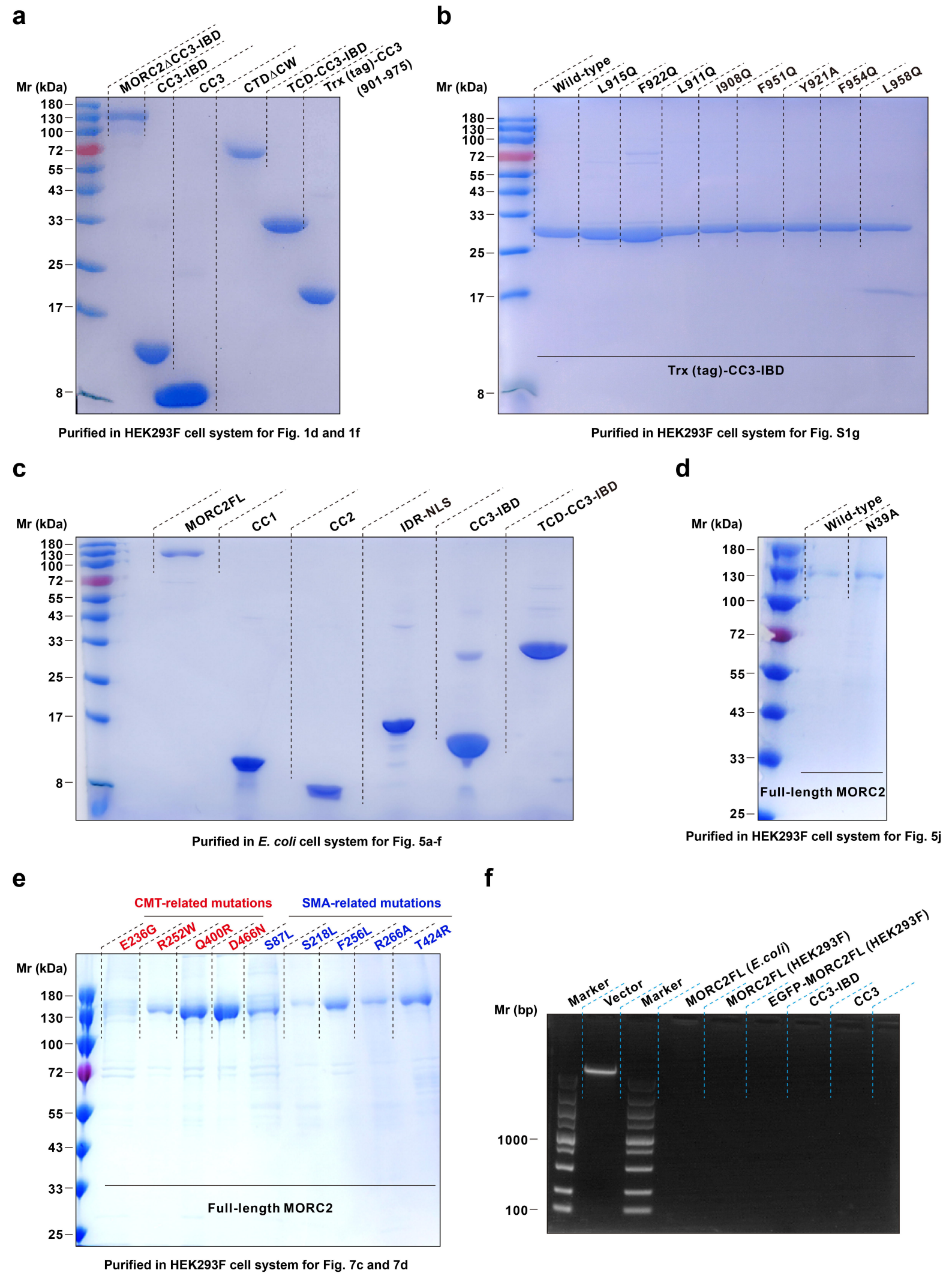
a
Mr (kDa)
MORC2ΔCC3-IBD
CC3-IBD
CC3
CTDΔCW
TCD-CC3-IBD
Trx (tag)-CC3 (901-975)
180
130
100
72
55
43
33
25
17
8
Purified in HEK293F cell system for Fig. 1d and 1f
b
Mr (kDa)
Wild-type
L915Q
F922Q
L911Q
I908Q
F951Q
Y921A
F954Q
L958Q
180
130
100
72
55
43
33
25
17
8
Trx (tag)-CC3-IBD
Purified in HEK293F cell system for Fig. S1g
c
Mr (kDa)
MORC2FL
CC1
CC2
IDR-NLS
CC3-IBD
TCD-CC3-IBD
180
130
100
72
55
43
33
25
17
8
Purified in E. coli cell system for Fig. 5a-f
d
Mr (kDa)
Wild-type
N39A
180
130
100
72
55
43
33
25
Full-length MORC2
Purified in HEK293F cell system for Fig. 5j
e
CMT-related mutations
SMA-related mutations
E236G
R252W
Q400R
D466N
S87L
S218L
F256L
R266A
T424R
Mr (kDa)
180
130
100
72
55
43
33
25
Full-length MORC2
Purified in HEK293F cell system for Fig. 7c and 7d
f
Mr (bp)
Marker
Vector
Marker
MORC2FL (E.coli)
MORC2FL (HEK293F)
EGFP-MORC2FL (HEK293F)
CC3-IBD
CC3
1000
100